Masters Theses   Student Theses and Dissertations

Fall 2018

Development of a CFD model of the catalytic combustion of a microtube multi-mode propulsion system

Andrew Paul Taylor

DEVELOPMENT OF A CFD MODEL OF THE CATALYTIC COMBUSTION OF A

MICROTUBE MULTI-MODE PROPULSION SYSTEM

by

ANDREW PAUL TAYLOR

A THESIS

Presented to the Graduate Faculty of the

MISSOURI UNIVERSITY OF SCIENCE AND TECHNOLOGY

In Partial Fulfillment of the Requirements for the Degree

MASTER OF SCIENCE

in

AEROSPACE ENGINEERING

2018

Approved by

Dr. Lian Duan, Advisor
Dr. Joshua Rovey
Dr. David Riggins

ABSTRACT

This thesis presents the process and results of the development of a computational fluid dynamics (CFD) model in ANSYS Fluent 18.1 on the catalytic decomposition of a novel liquid monopropellant in a microtube in order to gain deeper insights than what is available through the experimental data. The CFD model was created using the Euler-Euler Multiphase model in conjunction with the Heterogeneous Reaction submodel. Such a choice of modeling setting was backed up by theory and benchmark computations on multiphase and compressible flow, shown in Section 3 and Appendix A. It was found that the previously determined one-step reaction mechanism in Berg and Rovey [15] was not sufficient for Fluent due to a small mass imbalance; therefore, a new equation with trace species was calculated in NASA CEA to overcome this issue, and its accuracy was confirmed through a single phase Fluent case. From this case, the largest %diff between them was in the c_p at 6.7%, which was determined to be due to different calculation methods; the remaining tracked properties were all within 1%. The pressure drop was noted to be much smaller than expected, along with the outlet being subsonic, which was initially accounted to a lack of multiphasic effects. The multiphase simulations encountered solution issues, providing physically impossible values, divergence, or convergence only upon removal of combustion. The most likely cause of this error was hypothesized to be numerical approximations to the unknown steady state boundary condition in the monopropellant's experiment. It was determined that the multiphase effects could be approximated via a source term simulation, which built on the single phase case. This simulation also showed a smaller pressure drop, as well as an outlet Mach of 0.0895, leading to the conclusion that the outlet flow is subsonic. Given that the existing simulations cannot match all the desired quantities in the experiments, additional simulations with better designed numerical models and boundary conditions are necessary for them to fully explain the experiments.

ACKNOWLEDGMENTS

TABLE OF CONTENTS

LIST OF ILLUSTRATIONS

LIST OF TABLES

NOMENCLATURE

Symbol	Description
	Roman
AAN	Aliphatic Amine
A_c	Cross-Sectional Area
ADN	Ammonium Dinitramide
AN	Ammonium Nitrate
A_r	Pre-Exponential Factor
$[Bmim][dca]$	1-Butyl-3-Methylimidazolium Dicyanamide
$[Bmim][NO_3]$	1-Butyl-3-Methylimidazolium Nitrate
BRL	Ballistics Research Laboratory
$[C]$	Molar Concentration
c_p	Specific Heat at Constant Pressure
CP	Chemical Propulsion
c_v	Specific Heat at Constant Volume
CV	Control Volume
C_{vm}	Virtual Mass Coefficient
C_{wl}	Wall Lubrication Coefficient

d	Pipe Diameter
d_b	Bubble Diameter
$\mathcal{D}_{jk}$	Binary Mass Diffusion Coefficient of species j in species k
$D_{j,m}$	Mass Diffusion Coefficient
$D_{T,j}$	Thermal (Soret) Diffusion Coefficient
E	Energy
$[Emim][EtSO_4]$	1-Ethyl-3-Methylimidazolium Ethyl Sulfate
$[Emim][Im]$	1-Ethyl-3-Methylimidaolzium Bis(trifluoromethylsulfonyl)imide
Eo	Eotvos Number
EP	Electric Propulsion
E_r	Reaction Activation Energy
F	External Body Force
f	Friction Factor
f_{inc}	Incompressible Friction Factor
F_{lift}	Lift Force
F_{td}	Turbulent Dispersion Force
F_{vm}	Virtual Mass Force
F_{wl}	Wall Lubrication Force
g	Gravity
h	Sensible Enthalpy

h_Q	Heat Transfer Coefficient
HAN	Hydroxylammonium Nitrate
I	Unit Tensor
I_d	Density Impulse
ID	Inner Diameter
IL	Ionic Liquid
$IRFNA$	Inhibiting Red Fuming Nitric Acid
I_{sp}	Specific Impulse
$\vec{J}$	Diffusion Flux
k	Thermal Conductivity
k_b	Backward Reaction Rate
k_f	Forward Reaction Rate
K_{pq}	Interphase Momentum Exchange Coefficient
K_r	Equilibrium Constant
L_e	Entry Length
L^*	Sonic Length
M	Mach Number
$\dot{m}$	Mass Flow Rate
$\vec{n}$	Unit Normal Vector
NTO	Nitrogen Tetroxide

Nu	Nusselt Number
$O_{(\cdot)}$	Source Term
P	Perimeter
p	Pressure
$PFRM$	Plug Flow Reactor Model
Pr	Prandtl Number
Q	Intensity of heat exchange
q	Heat Flux
R	Radius
r	Radial Position
Re	Reynolds Number
$\hat{R}$	Molar Rate of Creation/Destruction
R_j	Net Rate of Production of Species j
R_r	Reaction Rate
r_{rec}	Recovery Factor
$RTIL$	Room Temperature Ionic Liquid
$\mathcal{R}$	Universal Gas Constant
S	Entropy
T	Temperature
t	Time

$TEAN$	Triethanolammonium Nitrate
UDF	User Defined Function
URF	Under-Relaxation Factor
V	Volume
v	Velocity
$\dot{V}$	Volumetric Flow Rate
v_f	Volume Fraction
v_{pq}	Interphase Velocity
MW	Molecular Weight
x	Axial Position
X	Mole Fraction
Y	Mass Fraction
y_w	Distance from the Wall

Greek

α	Thermal Diffusivity
β_r	Temperature Exponent
η	Rate Exponent
Γ	Third Body Effects
λ	Bulk Velocity

μ	Molecular Viscosity
ν	Stoichiometric Coefficient
ϕ	Mixture Composition
ϕ_{eq}	Equivalence Ratio
ρ	Density
σ	Surface Tension Coefficient
$\bar{\bar{\tau}}$	Stress Tensor
γ	Ratio of Specific Heats

Subscripts

atm	Atmospheric
b	Bulk (solid) Species
eff	Effective
fd	Fully Developed
g	Gas Phase
h	Heat
j	Species *j*
m	Mean
nondim	Nondimensionalized
o	Stagnation Conditions

op	Operating Condition
prim	Primary Phase
q	q^{th} phase
r	Radial Component
ref	Reference Case
sec	Secondary Phase
s	Surface-Adsorbed (Site) Species
t	Turbulent
th	Thermal
w	Wall
x	Axial Component
z	Swirl

Superscripts

$'$	Reactant
$''$	Product
0	Initial
1	Final
$*$	Sonic

1. INTRODUCTION

This thesis presents work done on the development of a Computational Fluid Dynamics (CFD) analysis over the catalytic decomposition of a novel ionic liquid monopropellant blend in a microtube multi-mode thruster. This paper goes on to explain the development of the CFD model, what results were obtained, and their relevance in terms of this thruster setup, as well as possible future work, such as developing a physics-based model of the inner mechanisms. In Section 1 of this paper, similar works in this field will be used to explain where multi-mode propulsion and CFD are as a whole, both apart and together, exemplifying progress so far, and how the analysis performed for this thesis fits into and expands said field. Section 2 will be devoted to describing the motivation for the model development in terms of its benefits over previous work.

The catalytic decomposition analyzed in this paper is a complex, multi-physics process including phenomenon such as gas phase chemical kinetics; surface catalytic reactions and gas-surface interactions; and phase change. To model such a complex system of processes, Section 3 will go into the model developed in ANSYS Fluent to analyze the setup, such as the specific models used to account for multiphase and combustion, and the calculations done in the background. Additionally, the high complexity of this simulation makes it necessary to test validation through a systematic benchmark validation procedure, where the constituent parts are proven individually and then integrated into the whole. This process is detailed in Appendix A.

Sections 4 and 5 will detail modeling setup, results, and discussion thereof of the simulations executed for the objectives of this thesis, namely a single phase case to prove a new reaction mechanism, a single phase case to highlight multiphasic effects, and a

multiphase case to compare to experimental results. The results of these will be compared to appropriate data, and the discussions will go into detail about the insights gained from the aforementioned results.

1.1. MULTI-MODE PROPULSION SYSTEMS

A Multi-mode (or Dual-mode) propulsion system is one in which a single spacecraft utilizes two or more propulsive systems, usually a high specific impulse mode, typically via electric thrusters, and a high thrust mode, typically chemical thrusters, through the use of common hardware and/or shared propellant. The main benefit of this type of system over traditional propellant systems is an increase in mission flexibility, due to the ability to choose the type of maneuver that best benefits the current objective [29]. An example of this is the Mars Global Surveyor, which made use of a bipropellant thruster in conjunction with aero-braking to enter orbit, and a monopropellant for attitude control [27]. It has also been shown that systems that combine both hardware and propellant (i.e., monopropellant systems) have additional mass savings compared to separate systems due to propulsion system hardware mass and unused oxidizer leftover from electric propulsion (EP) modes [12]. Research has shown that a promising propellant source for such a system is ionic liquids [28].

Monopropellant propulsion is a propulsive system that uses a single propellant ignited to produce an energy release, leading to high temperature and pressure exhaust gases being propelled through nozzle to produce thrust (Figure 1.1). Monopropellants are required to be both storable and readily ignitable, which causes them to require an external source (typically a catalyst or thermal ignition source) to decompose the monopropellant down to its more volatile parts from a nonspontaneously ignitable state, allowing the ignition process to begin. In catalytic combustion, the monopropellant is sprayed onto a heated catalyst (typically either a wall coating or honeycomb-like structure inserted in the early sections of the tube length) to begin the decomposition [12].
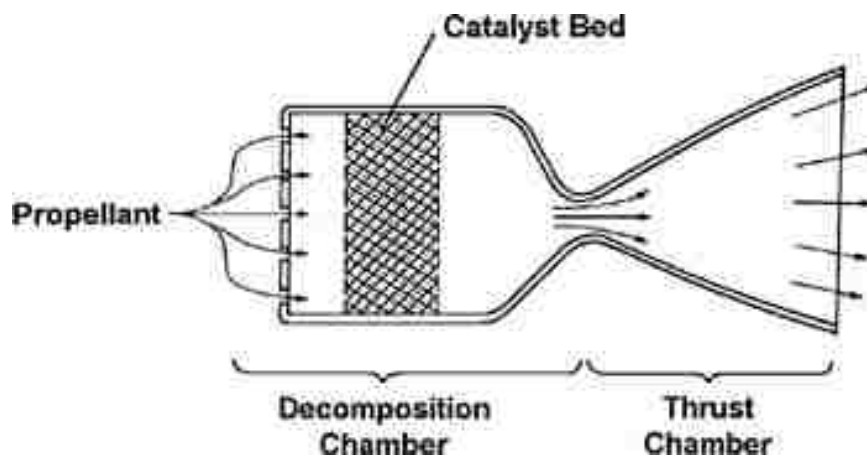
Figure 1.1. Simplified Monopropellant Thruster [12].

Ionic Liquids (ILs) are organic or inorganic salts in a molten (liquid) state. This molten state causes dissociation of cations and anions, but the liquid itself remains quasi-neutral. These ionic liquids are characterized by high thermal conductivity (k), high viscosity (μ), and low vapor pressure. A subgroup of ionic liquids exists called room temperature ionic liquids (RTIL's), which are liquid at or below 293 K [28]. From a propulsive standpoint, ionic liquids paired with the energetic salt Hydroxylammonium Nitrate (HAN) have been shown to have specific impulses (I_{sp}) of only 1-4% less than that of hydrazine, the most common monopropellant currently in use, while also being "green" propellants, which are becoming more and more desirable [12]. Additionally, multi-mode systems using ionic liquids are capable of higher ΔV than these traditional systems at the cost of burn time. One such system showed that, for an 80% EP ΔV, a HAN electrospray system produced 190% more ΔV than a hydrazine/xenon Hall effect thruster system, but at the cost of a 750% time increase [28].

Hydroxylammonium Nitrate, also called Hydroxylamine Nitrate (HAN), is an energetic salt that has been getting more attention recently due to events such as NASA's Green Propellant Infusion Mission, as it is a promising substitute for hydrazine on account of its high density and specific impulse, and relatively low toxicity. Due to being an unstable

solid crystal in its pure form, HAN is typically in an aqueous solution, such as the 24% wt. solution available from Sigma Aldrich. It is often blended with other compounds such as Triethanolammonium Nitrate (TEAN), methanol, or glycerol to improve performance [12].

Early work with HAN as a propellant was performed at the Army Ballistics Research Laboratory (BRL) toward developing a liquid gun propellant [26]. Decker et al. performed experiments to calculate physical properties such as density, viscosity, vapor pressure, electrical conductivity, and low temperature behavior for aqueous blends of HAN and TEAN at varying molarities, HAN-water-AAN (Aliphatic Amine) blends, and two proposed liquid propellants LGP 1845 and 1846, which were comprised of HAN-water-TEAN blends. This work prompted further examination into aqueous HAN solutions, such as Sassé [37], which examined the thermal characteristics of aqueous HAN, such as boiling temperature/behavior and heat of vaporization at different molarities, and Sassé et al. [39], which experimentally determined a second-order relation between HAN molar concentration and density. Results from these and other analyses were combined and summarized in [38].

Lee and Litzinger [32] developed a new reduced mechanism for thermal decomposition of HAN in an attempt to find a model that improves upon the two proposed models of the time from Oxley and Brower [1] and Klein [2], which varied in their choice of reacting species, resulting in differing condensed phase mole fractions. To accomplish this, the authors calculated Arrhenius rates through "an inverse-based iterative fitting technique." [32]. The determined reduced mechanism was very similar to the one proposed by Oxley and Brower [1], however several equations were changed to better account for the production of NO_2.

Amrousse et al. [11] performed a study on the thermal decomposition of HAN-based mixtures for their potential to replace hydrazine in spacecraft propulsion systems. The authors tested several different HAN-based solutions, with additional focus on a blend of HAN, Ammonium Nitrate (AN), water, and methanol (73.6/3.9/6.2/16.3 %wt) in order to determine the temperature onset and gas phase temperatures of the solutions; burning

rates and combustion temperatures; outlet gas products; and the effect of methanol addition on the aforementioned measured properties. Using a strand burner to catalytically combust the various solutions, it was determined that, overall, this HAN-based monopropellant is a viable hydrazine substitute. Additionally, it was determined that a 20% Ir catalyst performed very well and is a potential substitute for the Shell 405 catalyst (the standard catalyst for hydrazine), which can encounter issues at high temperatures, and that the preferred mixture performed with the best burning rates, although all mixtures performed better at elevated pressures [11].

Chambreau et al. [23] focused on the catalytic decomposition of HAN (a more recent focus of HAN-based research), seeking to determine the secondary products of HAN on an Ir catalyst in order to identify any important intermediate species that will contribute to the decomposition of HAN-based monopropellants. By using a copper plate for thermal decomposition and an iridium plate for catalytic decomposition, aerosolized HAN was vaporized into a vacuum chamber and measured by a mass spectrometer to determine products. From this, it was determined that the catalytic combustion enhanced the formation of NO and OH and produced an insignificant amount of NO_2, which was one of the expected products according to the thermal mechanism proposed by Lee and Litzinger [32] [23].

The findings of Donius and Rovey [28] were further fleshed out by Berg and Rovey [14] [16]. Imidazole-based ILs 1-Butyl-3-Methylimidazolium Dicyanamide ([Bmim][dca]), 1-Butyl-3-Methylimidazolium Nitrate ([Bmim][NO_3]), and 1-Ethyl-3-Methylimidazolium Ethyl Sulfate ([Emim][EtSO$_4$]) were tested for propellant performance in both CP and EP as monopropellants, bipropellants with oxidizers HAN, NTO, and IRFNA, and as binary mixtures with HAN modes against both hydrazine and FLP-103, an ADN-based monopropellant that is another possible alternative to hydrazine. Utilizing the NASA Chemical Equilibrium with Applications (CEA) code to calculate I_{sp}, density impulse I_d, and storability compared to hydrazine, it was found that while the monopropel-

lants and bipropellants did not perform as well as the hydrazine-NTO, the binary mixtures with HAN had roughly similar performance when blended to a combustion temperature of 1900 K, the technology limit as of publishing. Additionally, it was determined that these binary mixtures perform very well in electrospray, but would required a larger number of emitters than pure IL fuels, due to the lower molecular weight [14].

The performance of the Emim/HAN blend was tested against many systems in both a CP and EP capacity, such as Freon-14 and butane cold gas thrusters [17] [19], AF-M315E (A HAN-based monopropellant and popular choice for NASA's Green Propellant Infusion Mission), Teflon, 1-Ethyl-3-Methylimidaolzium Bis(trifluoromethylsulfonyl)imide ([Emim][Im], the only IL used for electrospray as the paper's publishing) [17], and specially formulated fuels such as Emim/HAN with small amounts of Fe_3O_4, which has "the potential to reduce system hardware complexity and power requirements in both... propulsive modes" [13], and a specially formulated choline nitrate-glycol mixed with either HAN or ammonium nitrate (AN) as an oxidizer, which was developed to outperform the Emim/HAN blend [33]. From these tests, it was generally determined that the Emim/HAN blend performed either near or above the other systems, especially after taking into account the mass reduction from common hardware and propellant.

Two rounds of catalytic testing on the Emim/HAN blend were performed via spot plate experiments, the first on rhenium, tungsten, and iridium [15], the second on platinum, rhenium, and titanium [18]. It was found from these tests that the Emim/HAN blend decomposes best on platinum at 85 °C, compared to the thermal decomposition temperature of 165 °C, and rhenium decomposition temperature of 125 °C. Arrhenius reaction rates were determined for these catalytic reactions. While there was initially concern for the melting of platinum, as the combustion temperature of 1900 K is above the sintering temperature, it was determined that this could be solved most easily through the addition of more fuel to the blend, which would lower the combustion temperature[18].

1.2. CFD ANALYSES

Recent work in the field of CFD analyses on microtube combustion has mainly been focused on the goals of either micropropulsion or power generation. An example is Boyarko, Sung, and Schneider [22], who experimented with the catalytic combustion of premixed H_2-air in platinum microtubes of 0.4 and 0.8 mm ID with the goal of "evaluation of the minimum catalyst temperature for initiating/supporting combustion in sub-millimeter diameter tubes, whose geometries approach or are smaller than the flame thickness of the propellants." In addition, they had a thruster performance goal of a I_{sp} of 300 sec, thrust between 1 and 10 mN, and a mass flow rate between 0.00034 g/s and 0.0034 g/s, all of which they succeeded in showing. Additionally, a plug flow model was used in order to determine a critical ignition heat flux, from which it was determined that "a well-engineered micro-combustor design should have power requirements less than 1 W and should self sustain once combustion is established" [22] and was able to achieve ignition in the latter half of the tube with a heat flux of 0.925 W/cm^2. This and other similar works were expanded upon in Volchko et al. [41], in which similar tests were performed on a rich premixed CH_4-air mixture in hopes of application to the NASA Mars initiative, which planned on using the CO_2 in Mars' atmosphere to create methane for return flights. In addition to physical experiments, Volchko also used the PLUG code in conjunction with the experimental data to provide more insight on the mechanics of the combustion. From the physical experiments, it was found that all tested conditions resulted in significant surface reactions (provided a high enough heat flux was applied) which were typically self-sustaining, and that heat flux, mass flow rate, and inlet pressure changed the location of ignition and its characteristics. From the PLUG flow simulation, a critical ignition temperature dependent only on equivalence ratio ϕ_{eq} and inlet pressure p_i [41] was determined. Until this critical temperature, the surface was dominated by $O(s)$. After this critical temperature, the surface species changed to

mainly $C(s)$ and $Pt(s)$, which facilitates the combustion of CH_4 and O_2, leading to product species formation [41]. As with Boyarko [22], Volchko found that microthrusters could be designed for as little as 1 W of provided power resulting in ignition [41].

Ranjan et al. [35] performed experiments and simulations to determine the viability of using the gas used to pressurize the liquid fuel of a microthruster as cold gas propellant in a 28° converging-diverging nozzle geometry in order to extend the life of a CubeSat in the 1-50 kg mass range. Selecting compressed air as a gaseous propellant, eight numerical simulations were performed at different feed pressure ratios (1-4 bar), split evenly between atmospheric and vacuum environmental conditions, and validated against experimental tests in both scenarios. For all scenarios, thrust and I_{sp} were tracked, and for simulations, contours of Mach Number along with axial Mach Number plots were generated. From these, it was determined that the thrust generated in vacuum was approximately twice as high in for each pressure ratio than in standard atmosphere, with the largest thrust value being approx. 2.24 mN at a 4 bar feed pressure in vacuum conditions.

For the goal of using micro-combustors for power generation, it has been found that "recent advances in the field of silicon micro fabrication techniques and silicon-based MEMS (micro-electromechanical systems) have led to the possibility of a new generation of micro heat engines for power generation" [25]. Chen et al. [24] investigated the influence of wall thermal conductivity k and inlet velocity on the catalytic combustion of H_2 and air inside a microtube through utilization of Fluent coupled with CHEMKIN software for the detailed reaction mechanism. Three cases were analyzed: just surface chemistry, just gas phase reactions, and both. From this, it was determined that the surface catalytic combustion restrains the gas phase due to consumption of a portion of the fuels, but also enhances the remaining gas phase reactions by producing high temperatures and radicals. Additionally, it was found that the microtube could be divided into two regions: an upstream region, where surface catalysis dominates, and a downstream region, where the gas phase dominates. It was discovered that a higher wall temperature gradient "promotes [a] gas phase combustion

shift upstream, and will result in a higher temperature distribution" [24]. Conversely, an increase in inlet velocity extends the surface catalysis region downstream, with a large enough increase causing this region to occupy the whole domain. In 2014, Chen, Yan, and Song [25] performed a similar experiment, in which Fluent 6.3.26 and DETCHEM 2.5 were used to analyze not only the same geometry and parameters, but also the effect of tube diameter on the combustion characteristics. While keeping a constant length to inlet diameter (L/d) of 16, an inlet diameter to tube diameter (d_{tube}/d) ratio of 2, and a constant wall thickness of 0.1 mm, the inlet diameter was varied to 0.2 mm, 0.4 mm, and 0.8 mm, as opposed to the earlier test, which held a constant 0.4 mm. It was determined that a decrease in tube diameter decreases the temperature of the flame core, as well as enhances the surface catalytic reactions, due to a higher surface area to volume ratio. Additionally, three characteristic reaction types were determined for micro-catalytic combustors: In the first, the gas phase is weakened by the surface catalytic reactions, but can be sustained by a large inlet velocity; in the second, the gas phase becomes unsustainable, while the surface catalysis becomes dominant; in the third, the gas phase can be completely neglected.

Similar H_2-Air CFD work was also performed by Shabanian, Rahimi, Khoshhal, and Alsairaft [40], in which the effect of reactant flow rates, combustor size, wall conductivity, and splitting of the H_2 feed on flame location, stability, and combustor performance was examined. In this simulation, the combustor was modeled using a 3D simulation, as opposed to the traditional method of an axisymmetric 2D simulation, in order to "not neglect the circumferential changes of velocity, temperature, species concentration, as well as heat and mass fluxes" [40]. It was found that only a range of mass flow rates provides stable combustion, with $\dot{m}$ too low causing quenching, and $\dot{m}$ too high causing blow out. It was also found that while a low wall thermal conductivity can reduce heat loss from the system, a large wall k increases the preheating of reactants and decreases the thermal stress of the wall. Lastly, hydrogen feed splitting was found to "cause a more uniform temperature to be established in in the chamber," which allows controls of combustor hotspots and leads to a

more efficient system [40]. In a similar vein of manipulating reactions for better stability and performance, Yan et al. [44] experimented with the effect of hydrogen addition to a preheated CH_4-air microcombustor to see its effect on reaction rate, ignition temperature, and stability in ANSYS Fluent. From these simulations, it was determined that adding a small amount of H_2 into the catalytic CH_4-air process has a significant effect by increasing reaction rate due to the hydrogen gas removing residual $O(s)$ from the walls, promoting the CH_4-Pt catalysis, lowering ignition temperature, and increasing stability of the combustion process.

2. PROBLEM DESCRIPTION

The overall goal of this work is to develop a numerical model that builds on and improves the initial modeling performed by Berg and Rovey [20], in which a 1D Plug Flow Reactor Model (PFRM) was used to define a 'startbox,' or range of initial conditions for successful ignition and self-sustained combustion, for the chosen propellant and geometry. In this setup, the geometry is a simple chemical microtube, defined as "a heated tube of diameter ~1 mm or less that may or may not consist of a catalytic surface material" (Figure 2.1) [20], such as the microtubes used in Boyarko et al. [22] and Volchko et al. [41], in which a novel blend of [Emim][EtSO$_4$]-HAN monopropellant decomposes using a one-step Arrhenius reaction, whose rate parameters were determined in previous work [18]. The PFRM model used by Berg was designed to determine the preheat temperature required to decompose the novel propellant for a defined length and flow rate of 15 μL/s (corresponding to a density ρ of 1420 kg/m^3 and a mass flow rate $\dot{m}$ of 21.3 mg/s), and was developed assuming a constant wall temperature, a pressure limit of 200 psia, 30 mm tube length, IDs of 400, 200, and 70 μm, and a preheat temperature ranging from 100°C to 343°C. In all cases simulated with this model, it was determined that decomposition occurred in less than 10 mm. An experiment was designed to validate these results, however it suffered from
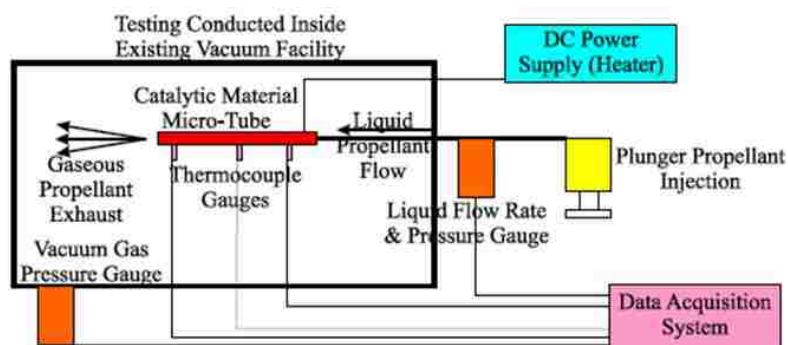
Figure 2.1. Experiment Schematic from Berg and Rovey [20].

the combustion ejecting the microtube from its friction fit housing, thereby preventing data acquisition for steady-state operation. It was determined from the limited experimental data that at ignition the inlet of the tube was approx. 100°C, and the PEEK tubing it was housed in provided a more isothermal condition than the rest of the tube, which caused the inlet to match fairly well with the simulation data.

While the PFRM is a simple model that is easy to implement and gives decent approximations, some assumptions made to simplify the equations can cause significant departure from reality in certain aspects. The two largest assumptions that are common among all PFR models are no boundary layer (inviscid flow) and no radial gradients in properties, such as velocity or temperature. Assumptions such as these can cause poor mixing of the component substances, which hinders combustion, and hot spots. Additionally, equations are simplified by using conditions that are not necessarily occurring, such as an isothermal or adiabatic wall. This particular decision was made in Berg and Rovey, and it was noted that "better heat transfer models are needed because the tube is far from the isothermal (condition) given the power to the tube was turned off and the thermal mass of the tube itself is low in comparison to the propellant thermal mass," and that "the models used to calculate these curves can be increased in fidelity or further refined" [20]. In order to increase the fidelity of this analysis, as well as account for the aforementioned effects, the simplest solution determined was to move the model into a commercial CFD software, in which the equations were able to capture all these and other phenomena, in order to obtain a more realistic flow model to compare future experimental testing against.

In addition to improving the 1D PFRM, the 2D CFD model proposed below also has other benefits over experiments, some of which are shared by simplified models such as the PFRM. Commonly referenced examples include [36] [4]:

- Low Cost: Performing simulations typically costs a fraction of the price of setting up and performing a scaled experiment of the same setup. Additionally, possible changes to the experiment can initially be modeled to determine the effect they would have.

- Speed: Most CFD simulations can typically be executed in a much shorter time frame, which allows the results to be used earlier in the design process and can hasten the time to manufacturing. It also allows quick feedback to possible design changes to determine feasibility of the change without requiring the process of experimentation.

- Simulation Ability: CFD can simulate idealized flows, as well as very complex physical processes that are very challenging to replicate in a testing environment (e.g. idealized adiabatic heat transfer, or hypersonic flow). This ability to isolate specific phenomena can assist design in determining the cause of issues with experimental setups.

- Comprehensive Data: While experiments only provide data at certain locations where measuring devices are placed (e.g., thermisters at set wall points or transducers at inlets/outlets), CFD simulations allow for insight into many properties at almost any point in the control volume (CV), which can help determine trends and mechanisms otherwise difficult/improbable via experimental measuring techniques alone.

In the present study, we choose the commercial package ANSYS Fluent 18.1 for analyzing microtube combustive flows. Fluent is a comprehensive CFD package that uses a form of the finite volume method to analyze a large variety of flow effects in both 2D and 3D, including turbulence, multiphase, reacting flows, acoustics, and heat transfer, as well as allowing user-defined functions (UDFs) for added customization. It supports parallel processing for increased convergence speed and comes with several programs for geometry and mesh generation as part of the package [10]. According to a survey by Resolved Analytics, it is the most popular CFD package used by a significant margin (Figure 2.2).

This ubiquity, as well as its superiority in handling complex flows, were the driving factors
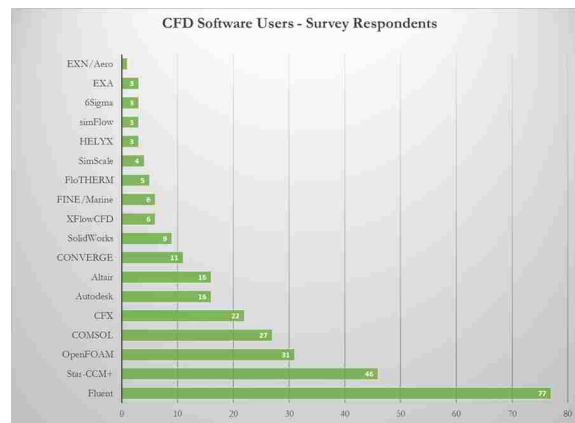
Figure 2.2. CFD Software Use Survey [8].

for its choice over similar packages like ANSYS CFX or OpenFOAM, as the thruster simulation uses the majority of the complex packages.

3. NUMERICAL METHODS

As previously stated, the processes being simulated for this analysis are several regimes of complex phenomena, and in order to validate the simulation properly, it must be tested as parts before it is tested as a whole. In this chapter, the ANSYS Fluent 18.1 models selected for use in the final simulations will be explained, both in reasoning for selection and in how they work. Additionally, benchmark cases for each regime are presented in Appendix A, showing both mastery over the use of each model, as well as its maturity for integration into the final simulation.

3.1. FLUENT MODELS

In order to build complex models in ANSYS Fluent, it is required to build them out of multiple smaller submodels. For example, simulating a turbulent, combusting flow requires a turbulence model, a species transport model, and the energy model. In this section, all of the submodels used by the final simulation are defined and explained, both in why they were chosen and the equations that show how they work.

3.1.1. Cold, Single Phase Fluid Flow. For every flow simulated on, ANSYS Fluent solves equations for conservation of mass (aka the continuity equation) and momentum (a form of the Navier-Stokes Equations). The basic forms used by Fluent are shown in Eqs. 3.1 and 3.2 below:

$$\frac{\partial \rho}{\partial t} + \vec{\nabla} \cdot (\rho \vec{v}) = O_{mass} \tag{3.1}$$

$$\frac{\partial}{\partial t}(\rho \vec{v}) + \vec{\nabla} \cdot (\rho \vec{v} \vec{v}) = -\nabla p + \nabla \cdot \bar{\bar{\tau}} + \rho \vec{g} + \vec{F} \tag{3.2}$$

where the stress tensor $\bar{\bar{\tau}}$ is defined as

$$\bar{\bar{\tau}} = \mu \left[(\nabla \vec{v} + \nabla \vec{v}^T) - \frac{2}{3} \nabla \cdot \vec{v} I \right] \tag{3.3}$$

Due to the 2D axisymmetric nature of the thruster geometry, these can be simplified, resulting in Eqs. 3.4 and 3.5:

$$\frac{\partial \rho}{\partial t} + \frac{\partial}{\partial x}(\rho v_x) + \frac{\partial}{\partial r}(\rho v_r) + \frac{\rho v_r}{r} = O_{mass} \tag{3.4}$$

$$\frac{\partial}{\partial t}(\rho v_x) + \frac{1}{r}\frac{\partial}{\partial x}(r \rho v_x^2) + \frac{1}{r}\frac{\partial}{\partial r}(r \rho v_x v_r) =$$
$$-\frac{\partial p}{\partial x} + \frac{1}{r}\frac{\partial}{\partial x}\left[r\mu(2\frac{\partial v_x}{\partial x} - \frac{2}{3}(\nabla \cdot \vec{v})) \right] + \frac{1}{r}\frac{\partial}{\partial r}\left[r\mu(\frac{\partial v_x}{\partial r} + \frac{\partial v_r}{\partial x}) \right] + F_x \tag{3.5a}$$

$$\frac{\partial}{\partial t}(\rho v_r) + \frac{1}{r}\frac{\partial}{\partial x}(r \rho v_x v_r) + \frac{1}{r}\frac{\partial}{\partial r}(r \rho v_r^2) =$$
$$-\frac{\partial p}{\partial r} + \frac{1}{r}\frac{\partial}{\partial x}\left[r\mu(\frac{\partial v_x}{\partial r} + \frac{\partial v_r}{\partial x}) \right] + \frac{1}{r}\frac{\partial}{\partial r}\left[r\mu(2\frac{\partial v_r}{\partial r} - \frac{2}{3}(\nabla \cdot \vec{v})) \right]$$
$$-2\mu\frac{v_r}{r^2} + \frac{2}{3}\frac{\mu}{r}(\nabla \cdot \vec{v}) + \rho\frac{v_z^2}{r} + F_r \tag{3.5b}$$

where

$$\nabla \cdot \vec{v} = \frac{\partial v_x}{\partial x} + \frac{\partial v_r}{\partial r} + \frac{v_r}{r} \tag{3.6}$$

Additional models, such as the ones described in subsequent sections, increase the complexity of the model and therefore add on additional equations to be solved.

3.1.1.1. Incompressible laminar liquid flow. For incompressible flows ($M \lessapprox$ 0.30), the density ρ variation is mostly negligible and can be treated as constant. This removes it as an unknown, making the equation system of Eqs. 3.4 and 3.5 an iteratively solvable system, assuming there is no swirl velocity. The setting of incompressible laminar flow is the default for ANSYS Fluent [5].

3.1.1.2. Compressible laminar gas flow. For gas flows with high velocities (roughly $M \gtrsim 0.3$) or high pressure variations ($\frac{\Delta p}{p}$), the density variation has a significant effect on velocity, temperature, and pressure. Typically the relation between these state variables is expressed via an equation of state (EoS), the most common of which is Ideal Gas Equation, shown in Fluent's form used below:

$$\rho = \frac{p_{op} + p}{\frac{\mathcal{R}}{MW}T} \tag{3.7}$$

where the operating pressure p_{op} is a term specified in the Fluent Operating Conditions Dialog Box, and is used to calculate gauge pressures. The default value of p_{op} is 1 atm, but it is recommended by the ANSYS User Guide to reduce the value to 0 Pa for compressible flows and input absolute pressures into the boundary conditions.

In order to close the system, an additional equation is needed. Fluent finds this in the form of the Conservation of Energy equation, with their form shown below:

$$\frac{\partial}{\partial t}(\rho E) + \nabla \cdot (\vec{v}(\rho E + p)) = \nabla \cdot \left[k_{eff} \nabla T - \sum_j h_j \vec{J}_j + (\bar{\bar{\tau}} \cdot \vec{v}) \right] + O_{energy} \tag{3.8}$$

where

$$E = h - \frac{p}{\rho} + \frac{v^2}{2} \tag{3.9a}$$

$$h = \sum_j Y_j h_j \tag{3.9b}$$

$$h_j = \int_{T_{ref}}^{T} c_{p,j}(T)dT \tag{3.9c}$$

keeping in mind that for higher temperatures in a fluid or large temperature changes, c_p cannot be assumed constant and must be calculated via other means, such as a polynomial curve fit, or through kinetic theory. This equation closes the system of Eqs. 3.4, 3.5, 3.7, and 3.8 to solve for v_x, v_r, p, ρ, and T [5].

3.1.1.3. Heated walls via imposed temperature or heat flux. Imposing a temperature condition on the walls is necessary for any flow simulation that requires use of the energy equation. In the scope of the multi-mode thruster, the walls fall on a boundary of the flow field, making the knowledge of the heat profile a necessary boundary condition. Typically, this is expressed in either a known temperature (Dirichlet) or heat flux (Neumann) profile, whether it is a constant value, an equation, or experimental data with interpolation between points; however, Fluent does offer additional options for declaring the thermal conditions on the boundaries, such as convection, radiation, and mixed [5].

3.1.2. Gas Phase Reaction Kinetics. For Laminar Combustion, ANSYS Fluent offers the Species Transport and Finite Rate Chemistry model, in which it solves the conservation equations with convection, diffusion, and reaction sources in order to model transport and mixing of chemical species. Fluent offers the ability to specify mixtures of up to 700 chemical species for reaction modeling, but contains several models that only work with up to 50 species. The local mass fraction of each species j of N total species is calculated via Eq. 3.10:

$$\frac{\partial}{\partial t}(\rho Y_j) + \triangledown \cdot (\rho \vec{v} Y_j) = - \triangledown \cdot \vec{J}_j + R_j + O_j \tag{3.10}$$

where, where the net species production rate R_j is defined in subsequent sections, and O_j is the creation rate from sources and additions from dispersed phases. For laminar flows, species j Diffusion Flux $\vec{J}_j$ is calculated using the Maxwell-Stefan Equations [5]:

$$\vec{J}_j = -\sum_{k=1}^{N-1} \rho D_{j,k} \nabla Y_k - D_{T,j} \frac{\Delta T}{T} \tag{3.11a}$$

where

$$D_{jk} = [D] = [A]^{-1}[B]$$

$$MW_m = \sum_{j=1}^{N} \frac{Y_j}{MW_m}$$

$$A_{jj} = -\left[\frac{X_j}{\mathcal{D}_{j,N}} \frac{MW_m}{MW_N} + \sum_{\substack{k=1 \\ k \neq j}}^{N} \frac{X_k}{\mathcal{D}_{jk}} \frac{MW_m}{MW_j} \right]$$

$$A_{jk} = X_j \left[\frac{1}{\mathcal{D}_{jk}} \frac{MW_m}{MW_k} - \frac{1}{\mathcal{D}_{jN}} \frac{MW_m}{MW_N} \right] \tag{3.11b}$$

$$B_{jj} = -\left[X_j \frac{MW_m}{MW_N} + (1 - X_i) \frac{MW_m}{MW_k} \right]$$

$$B_{jk} = X_i \left[\frac{MW_m}{MW_k} - \frac{MW_m}{MW_N} \right]$$

$$[A], [B], [D] = (N-1)x(N-1)$$

and

$$D_{T,j} = -2.59x10^{-7} T^{0.659} \left[\frac{MW_j^{0.511} X_j}{\sum_{j=1}^{N} MW_j^{0.511} X_j} - Y_j \right] \cdot \left[\frac{\sum_{j=1}^{N} MW_j^{0.511} X_j}{\sum_{j=1}^{N} MW_j^{0.489} X_j} \right] \tag{3.11c}$$

3.1.2.1. Volumetric reactions. While the Species Transport model can account for the Turbulence-Chemistry Interaction (TCI) in several different ways, the only available option for laminar reacting flows is Finite-Rate/No TCI. In this submodel, Fluent incorporates the finite-rate kinetics by computing chemistry source terms using general reaction-rate

expressions, such as the Arrhenius reaction rates, without attempting to account for the effects of turbulent fluctuations. The previously mentioned R_j source term is calculated as the sum of the sources over the N_R reactions that species j participates in [5]:

$$R_j = MW_j \sum_{r=1}^{N_R} \hat{R}_{j,r} \tag{3.12a}$$

where $\hat{R}_{j,r}$ is the Molar rate of creation/destruction of species j in reaction r, defined by

$$\hat{R}_{j,r} = \Gamma(v''_{j,r} - v'_{j,r}) \left(k_{f,r} \prod_{j=1}^{N} [C_{j,r}]^{\eta'_{j,r}} - k_{b,r} \prod_{j=1}^{N} [C_{j,r}]^{\eta''_{j,r}} \right) \tag{3.12b}$$

where the third body effect Γ is, by default, not included (i.e. given a value of 1). In this setup, ANSYS Fluent calculates the forward reaction rate using the Arrhenius equation (Eq. 3.13)

$$k_{f,r} = A_r T^{\beta_r} exp(-E_r/\mathcal{R}T) \tag{3.13}$$

and, if applicable, the backward reaction rate using either Eq. 3.14 or 3.15:

$$k_{b,r} = \frac{k_{f,r}}{K_r} \tag{3.14a}$$

where the equilibrium constant K_r is determined from

$$K_r = exp\left[\frac{\Delta S_r}{\mathcal{R}} - \frac{\Delta H_r}{\mathcal{R}T} \right] \left(\frac{p_{atm}}{\mathcal{R}T} \right)^{\sum_{j=1}^{N}(v''_{j,r} - v'_{j,r})} \tag{3.14b}$$

wherein the term in the exponential is representative of the change in Gibbs free energy, whose components are computed as shown:

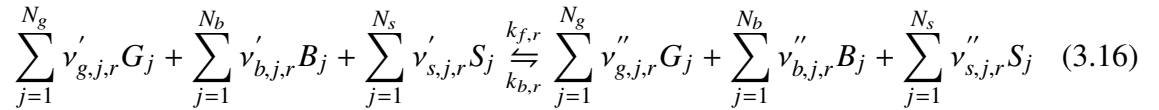$$\frac{\Delta S_r}{\mathcal{R}} = \sum_{j=1}^{N}(v''_{j,r} - v'_{j,r})\frac{S_j}{\mathcal{R}} \tag{3.14c}$$

$$\frac{\Delta H_r}{\mathcal{R}T} = \sum_{j=1}^{N} (v_{j,r}'' - v_{j,r}') \frac{h_j}{\mathcal{R}T} \tag{3.14d}$$

$$k_{b,r} = A_{b,r} T^{\beta_{b,r}} exp(-E_{b,r}/\mathcal{R}T) \tag{3.15}$$

where S_j and h_j represent the entropy and enthalpy of species j respectively at T and p_{atm}, and the variables in Eq. 3.15 have the same definitions as in 3.13, except the values are for the reverse reaction, as opposed to the forward. The choice of calculation method is left to the user [5].

3.1.2.2. Surface catalyst reactions. In addition to volumetric reactions, Fluent offers the ability to model reactions of the fluid with surfaces, including phenomena such as adsorption, desorption, and heat release. These reactions are defined and treated differently than the purely gas-phase reactions involving the same species, which is accounted for by the inclusion of both the solid and gaseous species for a material that participates in this class of reactions [7].

Consider the general form of the rth wall surface reaction:

$$\sum_{j=1}^{N_g} v_{g,j,r}' G_j + \sum_{j=1}^{N_b} v_{b,j,r}' B_j + \sum_{j=1}^{N_s} v_{s,j,r}' S_j \overset{k_{f,r}}{\underset{k_{b,r}}{\rightleftharpoons}} \sum_{j=1}^{N_g} v_{g,j,r}'' G_j + \sum_{j=1}^{N_b} v_{b,j,r}'' B_j + \sum_{j=1}^{N_s} v_{s,j,r}'' S_j \tag{3.16}$$

where G_j, B_j, and S_j are gas, bulk, and site species, respectively, N_g, N_b, and N_s are the number of species in each group, and the $v_{g,j,r}$, $v_{b,j,r}$, and $v_{s,j,r}$ are respective stoichiometric coefficients, with the superscript notation consistent with previous equations ($''$ for product, $'$ for reactant). Note that for reactions without certain classes of species, their stoichiometric coefficients will be zero, causing those terms in Eq. 3.16 to fall out, thus simplifying the equation.

The reaction rate of said r^{th} reaction is computed by

$$R_r = k_{f,r} \left(\prod_{j=1}^{N_g} [C_j]_{wall}^{\eta_{j,g,r}'} \right) \left(\prod_{k=1}^{N_s} [C_{s,k}]_{wall}^{\eta_{k,s,r}'} \right) - k_{b,r} \left(\prod_{j=1}^{N_g} [C_j]_{wall}^{\eta_{j,g,r}''} \right) \left(\prod_{k=1}^{N_s} [C_{s,k}]_{wall}^{\eta_{k,s,r}''} \right) \tag{3.17}$$

which is used in the $\hat{R}$ for the surface (Eq. 3.18):

$$\hat{R}_{j,g} = \sum_{r=1}^{N_{rxn}} \left(v''_{g,j,r} - v'_{g,j,r} \right) R_r, \quad i = 1, 2, 3, ..., N_g \tag{3.18a}$$

$$\hat{R}_{j,b} = \sum_{r=1}^{N_{rxn}} \left(v''_{b,j,r} - v'_{b,j,r} \right) R_r, \quad i = 1, 2, 3, ..., N_b \tag{3.18b}$$

$$\hat{R}_{j,s} = \sum_{r=1}^{N_{rxn}} \left(v''_{s,j,r} - v'_{s,j,r} \right) R_r, \quad i = 1, 2, 3, ..., N_s \tag{3.18c}$$

The rate constants k_f and k_b are calculated in the same manner as the gas-phase volumetric reactions, however the equilibrium constant contains an extra term to account for the reactions being on the surface, and the site density ρ_s of said surface:

$$K_r = exp\left[\frac{\Delta S_r}{\mathcal{R}} - \frac{\Delta H_r}{\mathcal{R}T} \right] \left(\frac{p_{atm}}{\mathcal{R}T} \right)^{\sum_{j=1}^{N_g} (v''_{j,r} - v'_{j,r})} \prod_{l=1}^{N_{types}} \left(\rho_s \right)_k^{\sum_{m=1}^{N_{s,l}} (v''_{k,l,r} - v'_{k,l,r})} \tag{3.19}$$

where N_{types} is the number of differing site types, and the stoichiometric coefficients are of the kth site species of type l in reaction r.

3.1.3. Multiphase Flow. While in nature, phases consist of solid, liquid, and gas, ANSYS Fluent uses a broader concept of the term. For multiphase flow in Fluent, "a phase can be defined as an identifiable class of material that has a particular inertial response to and interaction with the flow and the potential filed in which it is immersed" [5]. This means that a multiphase flow in Fluent is considered to be not only a domain with two of the standard phases, but also if there are differently sized particles of the same material in a flow, such as varying dispersed solid particles. Fluent divides multiphase flow into four regimes: gas-liquid or liquid-liquid; gas-solid; liquid-solid; and three-phase. In the case of a multi-mode thruster, the regime covered is gas-liquid (more specifically, bubbly or slug flow, shown in Figure 3.1), as the propellant enters in a liquid state, and is then vaporized and decomposed through catalytic combustion with the wall surface[7].

Figure 3.1. Bubbly Flow [7].

Fluent provides several options for multiphase models, with the most general classifications being Euler-Legrange and Euler-Euler. Euler-Legrange treats the fluid phase as continuum and solving Eqs. 3.1, 3.2, and 3.8, and tracks a number of particles in the dispersed phase [5]. As this method is not appropriate for situations where the second phase volume fraction is too large to be neglected (which is true in the case of the multi-mode thruster, as the liquid is completely decomposing into a gas), it was decided to use the Euler-Euler method instead.

In contrast, the Euler-Euler approach treats each phase as interpenetrating continua. It introduces a volume fraction $v_{f,q}$ for phase q, which is assumed to be a continuous function of space and time, with the sum of all phasic v_f equal to one. This is coupled with phasic conservation equations and constitutive relationships to get a closed system of equations. Typically, the constitutive relationships are obtained from empirical data. ANSYS Fluent has three different Euler-Euler models: The Volume of Fluid (VOF) model, which focuses on the interface between two immiscible fluids; The Mixture model, which solves for the mixture momentum equation and prescribes relative velocities to describe dispersed phases; and the Eulerian model, which is the most complex, and solves n momentum and continuity equations for each phase, coupling through the pressure and interphase exchange coefficients [5].

The ANSYS Fluent User's Guide gives a nine step general approach to solving multiphase flows [7]:

1. Enable the Multiphase model you want to use and specify the number of phases, as well as volume fractions scheme, if applicable.

2. Add the material representing each phase from the FLUENT Database, creating any materials needed that are not present.

3. Define the phases, and specify any interaction between them (i.e. surface tension, drag, mass transfer, etc.)

4. If the flow is Eulerian and turbulent, define the multiphase turbulence model. For this simulation, this step can be skipped.

5. Enable body forces, if applicable.

6. Specify the boundary conditions, including secondary-phase volume fractions at flow boundaries.

7. Set any model-specific solution parameters.

8. Initialize the solution and set the initial v_f for the secondary phases.

9. Calculate a solution and examine the results. Postprocessing and reporting of results are available for each phase selected.

Due to the presence of combustion, as well as the complex chemical structure of the propellant, it was decided to use the Eulerian Multiphase Model, as it will perform best, despite being a resource-intensive model. Additionally, as it is the liquid propellant that catalyzes with the wall into gaseous products, the heterogeneous reaction model will have to be incorporated into the simulation.

3.1.3.1. Euler-Euler multiphase flow. The Eulerian Model in ANSYS Fluent is solved by expanding on the standard equations of mass, momentum, and energy to account for each phase:

$$V_q = \int_v v_{f,q} dV \tag{3.20a}$$

where

$$\sum_{q=1}^{n} v_{f,q} = 1 \tag{3.20b}$$

Volume fraction v_f represents the space filled by each phase in the domain, and is used to connect system of equations for each phase together. It is calculated by Fluent from the continuity equation:

$$\frac{1}{\rho_{ref,q}}\left[\frac{\partial}{\partial t}(v_{f,q}\rho_q) + \nabla \cdot (v_{f,q}\rho_q \vec{v}_q) = \sum_{p=1}^{n}(\dot{m}_{pq} - \dot{m}_{qp})\right] \tag{3.21}$$

where $\rho_{ref,q}$ is the phase reference (volume averaged) density of phase q in the domain, $\dot{m}_{pq}$ and $\dot{m}_{qp}$ is the mass transfer from the secondary p^{th} phase to the primary q^{th} phase and back, respectively for all n secondary phases.

The momentum conservation for phase q is solved in Fluent by

$$\frac{\partial}{\partial t}(v_{f,q}\rho_q\vec{v}_q) + \nabla \cdot (v_{f,q}\rho_q\vec{v}_q\vec{v}_q) = -v_{f,q}\nabla p + \nabla \cdot \bar{\bar{\tau}}_q + v_{f,q}\rho_q\vec{g}$$

$$+ \sum_{p=1}^{n}\left[K_{pq}(\vec{v}_p - \vec{v}_q) + \dot{m}_{pq}\vec{v}_{pq} - \dot{m}_{qp}\vec{v}_{qp}\right] \tag{3.22a}$$

$$+(\vec{F}_q + \vec{F}_{lift,q} + \vec{F}_{wl,q} + \vec{F}_{vm,q} + \vec{F}_{td,q})$$

where K_{pq} is the momentum exchange coefficient, and $\vec{v}_{pq}$ is interphase velocity, whose value is dependent on the sign of $\dot{m}_{pq}$, in that if $\dot{m}_{pq} > 0$, then $\vec{v}_{pq} = \vec{v}_p$, and if $\dot{m}_{pq} < 0$, then $\vec{v}_{pq} = \vec{v}_q$. The converse is true for the relationship between $\dot{m}_{qp}$ and $\vec{v}_{qp}$. $\bar{\bar{\tau}}_q$ is defined as:

$$\bar{\bar{\tau}}_q = v_{f,q}\mu_q(\nabla\vec{v}_q + \nabla\vec{v}_q^T) + v_{f,q}(\lambda_q - \frac{2}{3}\mu_q)\nabla \cdot \vec{v}_q\bar{\bar{I}} \tag{3.22b}$$

where μ_q and λ_q are shear and bulk velocity of phase q, respectively. ANSYS Fluent provides several models to choose from to calculate the various force terms, depending on the application and domain. For the case of laminar heterogeneous catalytic combustion in a pipe, the following were used:

- $\vec{F}_{lift,q}$: Fluent includes a term for the effect of lift on the secondary phase, which is mainly caused by velocity gradients in the flow field of the primary phase. However, the inclusion of it is not recommended for closely packed particles or very small particles. Therefore, it was chosen to not include this term in the simulation.

- $\vec{F}_{wl,q}$: The effect of wall lubrication is to push the secondary phase away from the wall, causing a secondary phase concentration near, but not on, the wall. The Wall Lubrication Force is calculated from Eq. 3.23:

$$\vec{F}_{wl} = C_{wl} \rho_{prim} v_{f,sec} |(\vec{v}_q - \vec{v}_p)_{||}|^2 \vec{n}_w \tag{3.23}$$

where $|(\vec{v}_q - \vec{v}_p)_{||}|^2$ is the phase relative velocity component tangential to the wall. Fluent offers several ways to calculate the wall lubrication constant C_{wl}, of which was chosen the Tomiyama Model. The Tomiyama Model is an accurate model that is limited by its dependence on pipe diameter, so that it only applies to pipe flows, which applies to our case. It calculates C_{wl} using Eq. 3.24a:

$$C_{wl} = C_w \frac{d_b}{2} \left(\frac{1}{y_w^2} - \frac{1}{(D - y_w)^2} \right) \tag{3.24a}$$

where

$$C_w = \begin{cases} 0.47 & Eo < 1 \\ e^{-0.933Eo+0.179} & 1 \leq Eo \leq 5 \\ 0.00599Eo - 0.0187 & 5 < Eo \leq 33 \\ 0.179 & 33 \leq Eo \end{cases} \tag{3.24b}$$

and Eo is the Eotvos Number, defined by

$$Eo = \frac{g(\rho_q \rho_p)d_b^2}{\sigma} \tag{3.24c}$$

and σ is the surface tension coefficient.

- $\vec{F}_{vm,q}$: In multiphase flows, a "virtual mass effect" can occur if a secondary phase accelerates relative to the primary phase. The inertia of the primary phase encountered by the accelerating particles exerts a "virtual mass force" on the particles, defined by 3.25a. This effect can be significant when the secondary phase density is much lower than the primary phase density, and therefore is included in the simulation.

$$\vec{F}_{vm} = C_{vm} v_{f,p} \rho_q \left(\frac{d_q \vec{v}_q}{dt} - \frac{d_p \vec{v}_p}{dt} \right) \tag{3.25a}$$

where the virtual mass coeff. C_{vm} is typically 0.5. $\frac{d_q}{dt}$ denotes the phase material time derivative:

$$\frac{d_q(\phi)}{dt} = \frac{d(\phi)}{dt} + (\vec{v}_q \cdot \nabla)\phi \tag{3.25b}$$

- $\vec{F}_{td,q}$: For turbulent multiphase flows, Fluent can account for interphase momentum transfer via turbulence effects through inclusion of turbulent dispersion forces. However, as the thruster flow is laminar, this term was neglected.

The energy equation for Eulerian Multiphase is as follows:

$$\begin{aligned}
\frac{\partial}{\partial t}(v_{f,q}\rho_q h_q) + \nabla \cdot (v_{f,q}\rho_q \vec{v}_q h_q) &= v_{f,q}\frac{dp_q}{dt} + \bar{\bar{\tau}}_q : \nabla \vec{v}_q - \nabla \cdot \vec{q}_q + O_q \\
&+ \sum_{p=1}^{n} \left[Q_{pq} + (\dot{m}h)_{pq} - (\dot{m}h)_{qp} \right]
\end{aligned} \tag{3.26}$$

where Q_{pq} is the intensity of heat exchange between phases p and q, and h_{pq} is interphase enthalpy. Interphase heat exchange must satisfy the local balance conditions of $Q_{pq} = -Q_{qp}$ and $Q_{qq} = 0$ [5].

3.1.3.2. Heterogeneous reactions. In ANSYS Fluent, species transport can be solved in multiphase by having ANSYS Fluent predict the local mass fraction $Y_{j,q}$ via solving the convection-diffusion equation for each species j in each phase q [5]. The species conservation equation can be adapted to Eq. 3.27 below:

$$\frac{\partial}{\partial t}\left(\rho_q v_{f,q} Y_{j,q}\right) + \nabla \cdot \left(\rho_q v_{f,q} \vec{v}_q Y_{j,q}\right) = -\nabla \cdot v_{f,q} \vec{J}_{j,q} + v_{f,q} R_{j,q} + v_{f,q} S_{j,q} +$$
$$\sum_{p=1}^{n} \left(\dot{m}_{p^j q^k} - \dot{m}_{q^k p^j}\right) + O_j \tag{3.27}$$

For multiphase reactions, by default ANSYS Fluent offers only Volumetric reaction mechanisms, but Wall and Particle Surface mechanisms can be simulated through UDFs. Additionally, Fluent accommodates both multiphase and single phase reactions in the same simulation, with the single phase scaled by its volume fraction v_f. The heterogeneous reaction model is compatible only with the laminar finite-rate, finite-rate/eddy-dissipation, and eddy-dissipation turbulence chemistry models [5]. Since the species model being used for the thruster is the laminar finite-rate, this model should have no issues being integrated.

For phase interaction rates, ANSYS Fluent allows both UDFs and a modified Arrhenius type rate expression (Eq. 3.28):

$$Rate = k \prod_{i=1}^{NR} \left(\frac{Y_i \rho_{ip} v_{f,ip}}{MW_i}\right)^{v_i} kmol/m^3 - sec \tag{3.28a}$$

where

$$k = A\left(\frac{T_{ip}}{T_{ref}}\right)^b exp\left(\frac{-E}{\frac{\mathcal{R}}{MW} T_{ip}}\right) \tag{3.28b}$$

NR is the number of reactants, and $(\cdot)_{ip}$ is for phase ip (e.g. T_{ip} is the phase temperature). T_{ref} is typically set to unity, but can be changed. Lastly, Eq. 3.28 will only be valid above a provided kick-off temperature provided by the user.

4. CFD FOR SINGLE-PHASE MICROTUBE COMBUSTION CASE

In this section, the single-phase combustion simulations are discussed. First, the setup of the model, including mesh details, Fluent models used, and boundary conditions are presented. The second section then presents the results and their comparison to experimental data and previous calculations. Lastly, these results are discussed in terms of explaining any disparities, and their overall impact to the project.

4.1. MODEL DESCRIPTION

The geometry of the model used in the subsequent simulations was based on the microtubes tested in the aforementioned experiment by Berg and Rovey [20], namely an inner diameter of 0.4 mm, a wall thickness of 0.15 mm, and a length that is expected to result in a sonic outlet via frictional/thermal choking. As the chief phenomenon experienced in the simulation was wall reactions, the mesh was designed to bias towards the inlet and the wall, which allowed a reduced overall element count and consequently a reduced computational time, while still capturing the important phenomena. In addition to this, Fluent was run in parallel on six processors to further reduce computational time.

As the thruster is cylindrical, the mesh was designed for an axisymmetric simulation, wherein a 2D mesh is rotated about a specified axis for analysis, which allows for a quasi-3D solution at a reduced calculation time from using only the mesh of half an axial cross section, with the only assumption being transversal uniformity, which is typical in cases like this. A mesh sensitivity study was performed (Table 4.1), which measured the number of iterations required to reach the final solution and the % Mass Imbalance for several meshes, and it was found that a mesh of 15 radial elements by 4,500 axial elements (totaling 67,500 elements) performed best for this simulation, both in computation time and imbalance accuracy (Figure 4.1).

Table 4.1. Mesh Sensitivity Study Results.

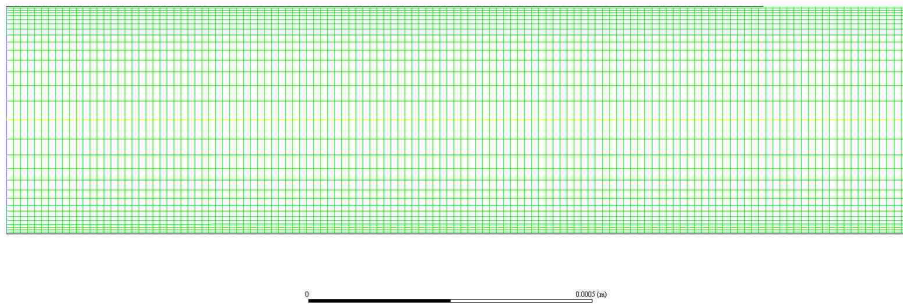| Element Ct.	Iter. to Solve	%Mass Imb.
100k (20x5,000)	244	5.55e-05
67.5k (15x4,500)	147	3.81e-05
61.2k (18x3,400)	152	5.43e-05

Figure 4.1. Close up of single-phase Microtube Mesh, Focused at the inlet.

The small diameter of the microtube resulted in a Reynolds Number (Re) in the laminar flow regime, so the laminar viscosity model was used in the simulation. Additionally, the Finite-Rate/no Turbulence Chemistry Interaction Species Transport model with wall surface reactions enabled was used to track the catalytic decomposition, which required the enabling of the energy equation. The species mixture was modeled as an ideal-gas mixture, which used the Ideal Gas Law to close the system of equations (Eq. 4.1).

$$P = \rho \frac{\mathcal{R}}{MW} T \tag{4.1}$$

Explanations of these models, along with benchmark simulations, are provided in Appendix 3. The Arrhenius rates used in this reaction model were elucidated in Berg and Rovey [18] and are shown in Eq. 4.2:

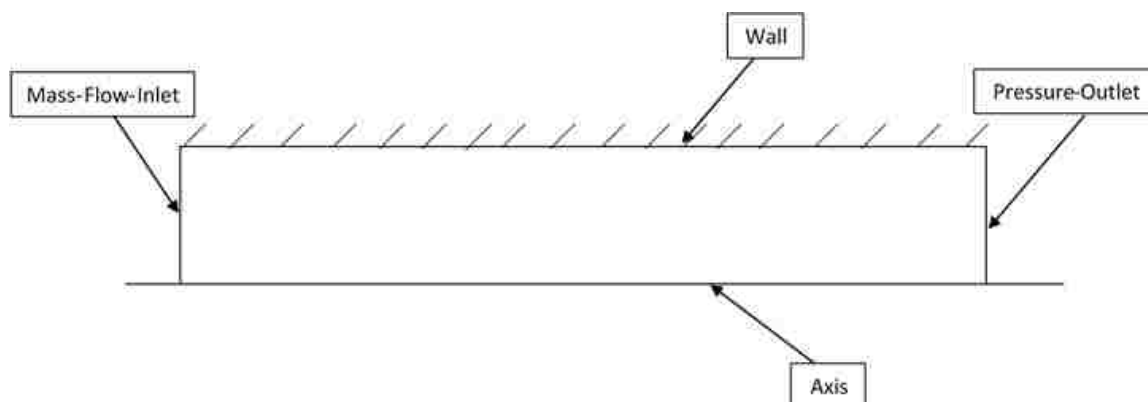$$-r_A = 2.14 * 10^{10} exp(\frac{-10771}{T})[C]_A \tag{4.2}$$

Figure 4.2. Diagram of Microtube BCs.

The boundary conditions used in the single-phase simulation consist of a mass-flow-inlet, pressure-outlet, adiabatic or radiative no-slip wall, and axis (Figure 4.2). More specifically, the volumetric flow rate of 15 μL/s was conserved, resulting in an inlet $\dot{m}$ of 0.7 mg/s and p_i of 200 psia at $T = 450$ K, and pressure at the outlet adjusted to achieve the correct inlet pressure, due to Fluent's treatment of pressure boundaries. The wall was adiabatic for the reaction mechanism confirmation simulation, and set to a wall emissivity ϵ of 0.05 with a free stream temperature of 300 K for the radiative position.

The simulation itself was run using the coupled pressure-velocity scheme, and solved first for first order spatial discretization to a residual tolerance of 1e-6, and then second order to the same tolerance. The field was initialized by using hybrid initialization, with the first 15% of the tube patched to the combustion temperature of 1900 K and a propellant mass fraction of 1.

4.2. RESULTS

The goal of the first single-phase simulation (the adiabatic wall case) was to further verify a new reaction equation for the decomposition of the novel monopropellant, as the original equation provided in Berg and Rovey [15] (Eq. 4.3 was found to have too large a
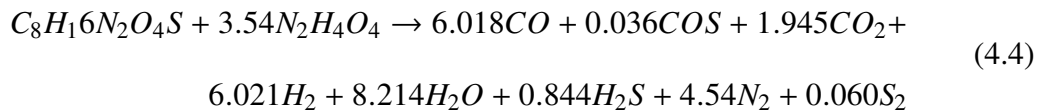
Table 4.2. Reaction Equation CEA Data Comparison.

Property	Old CEA[20]	New CEA	%Difference
T_c (K)	1900	1903.34	0.11758
γ	1.218	1.2341	1.3218
Mass %Diff	3.5742	2.78e-05	

mole disparity between the reactants and products for ANSYS Fluent to accept.

$$C_8H_{16}N_2O_4S + 3.54N_2H_4O_4 \rightarrow$$

$$1.87CO_2 + 6.10CO + 8.12H_2O + 6.46H_2 + 4.54N_2 + 0.47H_2S$$

(4.3)
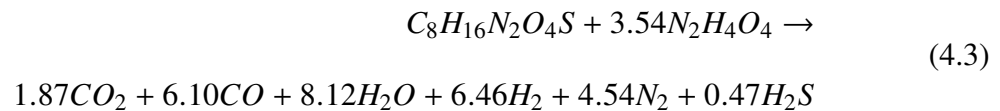
Utilizing the same case in the NASA CEA code, the cutoff tolerance for product species was lowered to 1e-4, and a new equation was formulated (Eq. 4.4), which was found to fit Fluent's tolerance:

$$C_8H_16N_2O_4S + 3.54N_2H_4O_4 \rightarrow 6.018CO + 0.036COS + 1.945CO_2+$$

$$6.021H_2 + 8.214H_2O + 0.844H_2S + 4.54N_2 + 0.060S_2$$

(4.4)

This new equation was first checked against the old CEA data for similarity (Table 4.2), as the properties were not expected to undergo drastic changes. The variance in values was deemed appropriately small, and the new equation failed to have any errors in Fluent when implemented.

From the adiabatic wall case, mean molecular weight MW, combustion temperature T_c, specific heat C_p, specific heat ratio γ, and sonic velocity u^* were compared at the outlet (shown in Table 4.3).

In the radiative wall case, the species mass fraction distribution (shown in Table 4.4), temperature, and Mach number were calculated at the outlet. In order to compare to the single values given in the NASA CEA output, the area-weighted average values of each

Table 4.3. CEA Property Comparison.

Property	NASA CEA	FLUENT	%Diff
MW (kg/kmol)	20.8190	20.8146	0.0213
T_c (K)	1903.34	1905.67	0.1126
Cp (kJ/kg-K)	2.1709	2.0238	6.7744
γ	1.2341	1.2459	0.9754
u^* (m/s)	968.5	973.9	0.5554

property were calculated at the outlet by Fluent. Average outlet temperature was calculated to be 1012.405 K, and average outlet Mach number was calculated to be 0.0023, which correlates to approx. 1.68 m/s.

Table 4.4. Outlet Mass Fraction Comparison

Species	Theoretical	FLUENT	%Diff
Prop	0	0	0
CO	0.2925	0.2926	0.0249
COS	0.0037	0.0037	0.0262
CO_2	0.1486	0.1486	0.0249
H_2	0.0211	0.0211	0.0248
H_2O	0.2568	0.2566	0.0721
H_2S	0.0499	0.0499	0.0249
N_2	0.2207	0.2208	0.0249
S_2	0.0067	0.0067	0.0246

The radially-averaged mass fraction evolution of the species (Figure 4.3) shows that the combustion begins within the first 10% of the tube length, which is in agreement with the simulation by Berg and Rovey [20]. Due to several products having a small mass fraction, a secondary plot is provided that allows easier viewing of the product mass fractions (Figure 4.4).

Additionally, the temperature of the wall, axis, and area-averaged slices were plotted against each other (red, black, and green, respectively) (Figure 4.5). The roughly linear behavior shown by the temperature profiles is in good agreement with theoretical/experimental
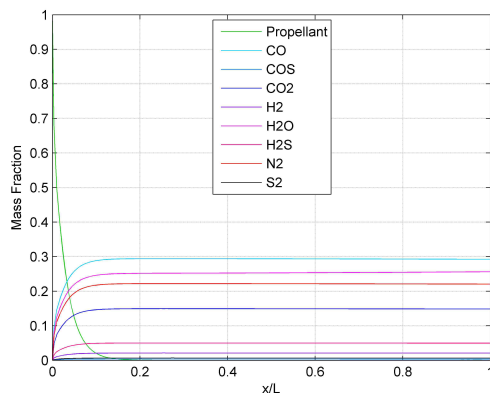
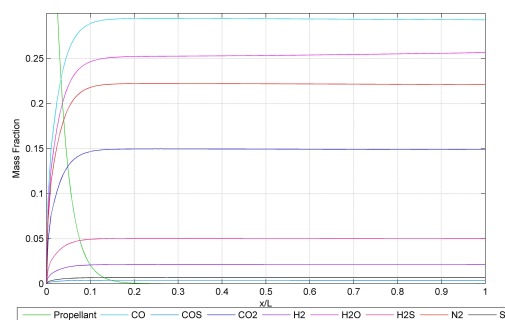Figure 4.3. Mass Fraction Distribution for Radiative Wall Case.
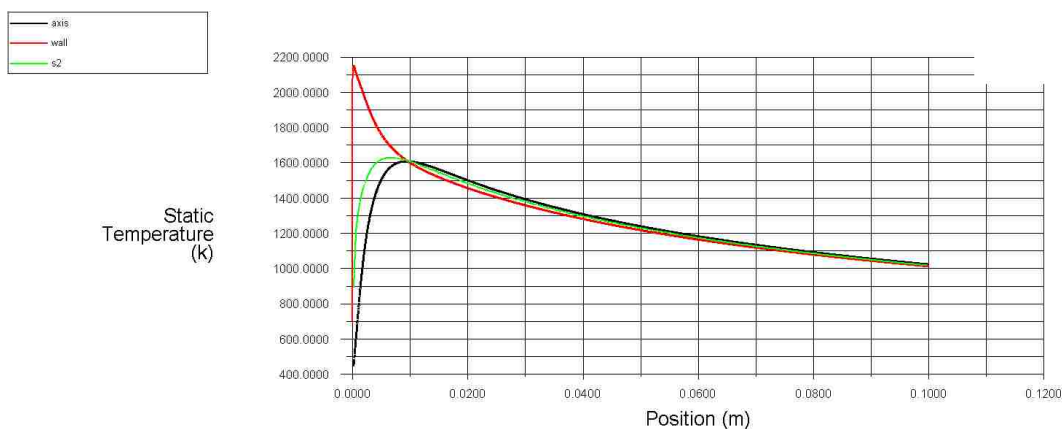

Figure 4.4. Zoomed View of Figure 4.3.

Figure 4.5. Temperature Profile of Wall, Centerline, and Average in Radiative Wall case vs. Axial position (m).

data. While the wall temperature has a spike of roughly 2127 K, which is above the expected combustion temperature, this behavior is expected of one-step reaction mechanisms and can also be seen when comparing one step and reduced mechanisms of hydrocarbons, such as methane.

For observation, several contours and plots have been included, highlighting the flow. Figure 4.6 shows the developing temperature due to combustion. Unfortunately, the length to width ratio of the microtube prevents showing of the entire tube in a visible manner. However, it can be observed from this inlet region the quick rise in temperature
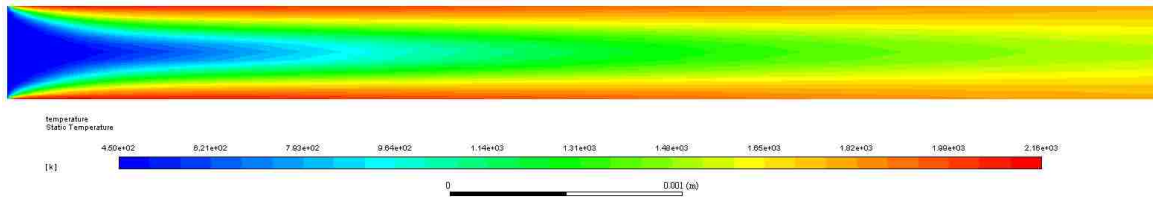
Figure 4.6. Temperature Contour of Radiative Wall case vs. Axial position (m), focused at inlet.

due to combustion, and the slow decrease due to the heat loss through the wall. Figure 4.7 displays the development of the velocity profile. The development in the inlet region varies from the typical developing profile, due to the heat added from combustion, however the flow reaches the fully developed Poiseuille flow condition relatively quickly once the bulk of combustion is complete. Figure 4.8 details the distribution of propellant mass
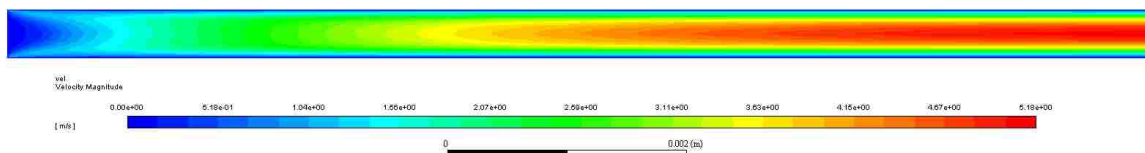
Figure 4.7. Velocity Contour of Radiative Wall case vs. Axial position (m), focused at inlet.

fraction y_j as it enters the thruster. It can be seen that the value drops to approx. 0.5 almost instantly at the walls, signifying combustion of the propellant immediately upon entering the thruster. Comparing this figure to Figure 4.7, it can be observed that the end of combustion correlates with the flow becoming fully developed. In order to better show this correlated development, radial profiles of propellant mass fraction and nondimensionalized
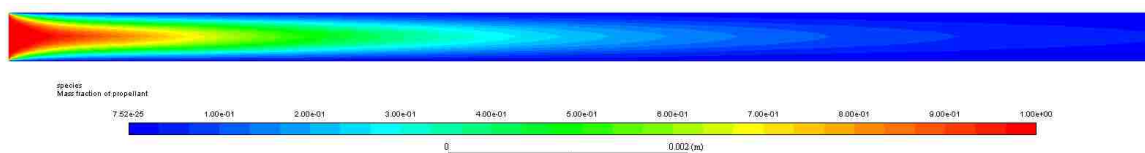

Figure 4.8. Propellant y_j Contour of Radiative Wall case vs. Axial position (m), focused at inlet.

flow velocity were plotted at several points along the radial body (Figures 4.9 and 4.10). From these plots, it can be clearly seen that the propellant mass fraction reducing to zero coincides extremely well with the flow becoming fully developed at $x/L = 20\%$.
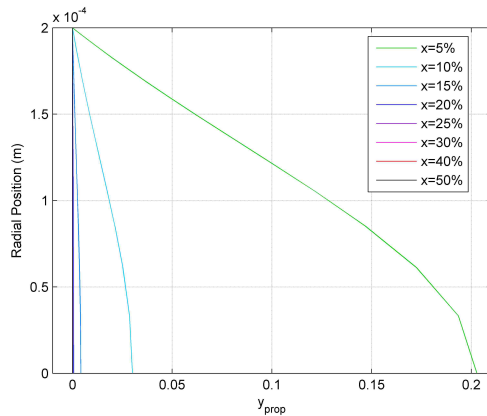

Figure 4.9. Radial Profiles of Propellant Mass Fraction.
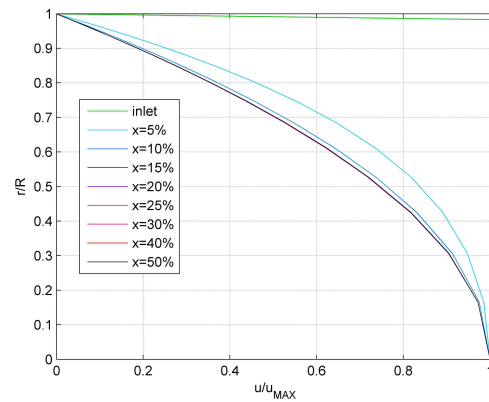
Figure 4.10. Radial Profiles of Nondimensionalized Flow Velocity.

4.3. DISCUSSION

From Tables 4.3 and 4.4, it can be observed that the simulation results correlate very well with the NASA CEA output, with the exception of the product c_p, which had the largest error of 6.77%. The most probable cause of this disparity was determined to be in the constants used to calculate c_p in the two programs. Upon examination, the two programs use different constants, but similar temperature ranges to calculate c_p for individual species. These two curves are plotted in Figure 4.11, and the disparity at the combustion temperature can be easily observed. The outlet velocity results are notably less promising. The Mach number of 0.0023 was far less than the roughly sonic condition expected, but this can be explained at least in part by the density formulation and lack of multiphasic effects. Due to defining the fluid as an ideal gas mixture, the density was defined from the ideal gas law (Eq. 4.1) instead of setting the inlet density by the incompressible density of the liquid propellant ($\rho_{propellant} = 1420\ kg/m^3$). This causes the inlet density to be 46.441 kg/m^3,

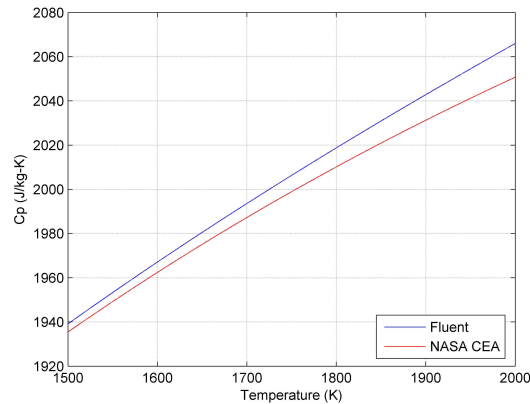Figure 4.11. c_p Curve Comparison between NASA CEA and Fluent.

roughly 30 times smaller than the propellant density. This lower density means there is less mass and momentum to be transferred from the reactants to the products ($\dot{m}$ was reduced by the same factor in order to match volumetric flow rate to the experiment), resulting in a smaller velocity post combustion and thus at the outlet. By defining two separate phases, one a liquid propellant with constant density, and one an ideal gas mixture of products, mass and momentum transfer can be properly represented, while still accurately defining the product mixture.

In the future, it is worth exploring the effect of adjusting other properties, to see how they affect the flow, particularly in the scope of bringing the single-phase closer to the experimental setup. One method for this would be to adjust the pressure such that Eq. 4.1 provides the proper density and therefore mass flow rate, and see the effect this has on the overall flow, especially at the outlet. Another would be a parametric study to determine the inlet mass flow rate required to achieve the sonic outlet condition desired. Such cases could also provide more insight towards the development of the multiphase case. Additionally, an extension of the domain to capture upstream of the catalytic wall is worth considering, as this should provide more insight on the ignition at the inlet.

5. CFD FOR MULTIPHASE MICROTUBE COMBUSTION CASE

Similar to Section 4, this section covers the modeling of the Multiphase Combustion Simulations. It begins with describing the model settings, with a focus on the additional settings and differences from the single phase case. Next, it shows the results obtained from said simulations, determines any sources of error, and explains the steps taken to remedy them. The final portion of this section discusses the importance of the results, and their overall contribution.

5.1. MODEL DESCRIPTION

As the multiphase simulation is designed to build upon the single phase case, the geometry of the domain is identical as previously described. The first round of multiphase simulations utilized the 100,000 element mesh referenced in Table 4.1, and is shown in Figure 5.1. Although many of the same models are used, additional models for multiphase, namely the Euler-Euler Multiphase model coupled with the Heterogeneous Reaction Model was used to incorporate the multiphasic effects. The denser model was chosen despite the study because multiphase modeling typically requires a denser mesh than single phase, due to the numerically difficult equations for phase interaction. For this simulation, the primary phase was defined as the gas phase, as it occupies the majority of the domain, and the secondary dispersed phase was the liquid propellant. The mixture definitions of the gas phase were the same as the single phase, with the exception of the removal of the propellant to add to the liquid phase. The liquid phase was defined using the volume-weighted-mixing law for density, as opposed to the ideal gas law formulation, and mass-weighted-mixing laws for other properties, thus defining the phase as an incompressible fluid, and conserving its density. The one-step Arrhenius reaction equation was run through the Heterogeneous Reaction model, which allows reactions between phases, as opposed to the wall surface
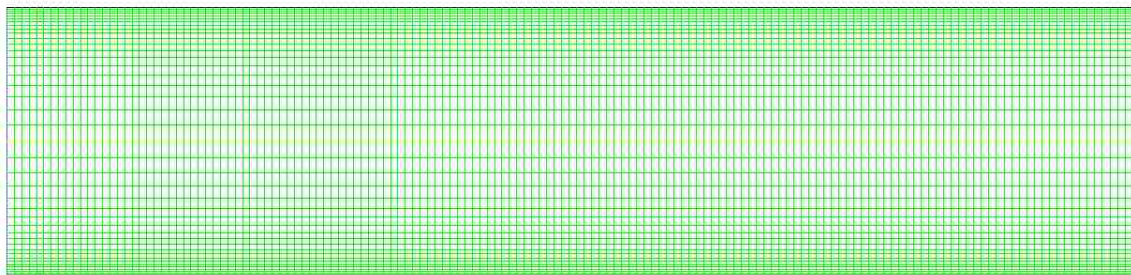
Figure 5.1. Close up of 100,000 Element Mesh.

homogeneous reaction settings, as previously used, as they do not. The simulation initially allowed the reactions to take place in the whole domain, with the plan being to restrict them to the walls using a UDF once an initial solution was found to converge, as heterogeneous wall reactions cannot be explicitly defined in Fluent, and require UDFs.

The boundary conditions for this first round was identical in type to the single phase (see Figure 4.2, with several of the specific values changed. Specifically, the inlet $\dot{m}$ was adjusted to 20 mg/s, the experimental $\dot{V}$ multiplied by the actual propellant density, and the volume fraction for the inlet was set to all liquid. The outlet pressure was set to sonic pressure p^*, and backflow volume fraction was set to all gas. For solution methods, the coupled pressure-velocity scheme was used, in conjunction with the pseudo-transient submodel, and first order spatial discretizations. The qualitative solution was set to a tolerance of 1e-3, with further refinements being applied at this point before moving to second order discretization and a smaller residual tolerance.

The second round of multiphase simulations was executed on the less dense mesh of 67,500 elements (Figure 4.1) used in the Single Phase Case, as it was found the memory required for the UDF was such that the 100,000 mesh cause a segmentation fault. This setup also changed the inlet condition to a velocity-inlet, as the flow was found to be subsonic enough that it was a valid option (Figure 5.2). The outlet pressure for this case was adjusted
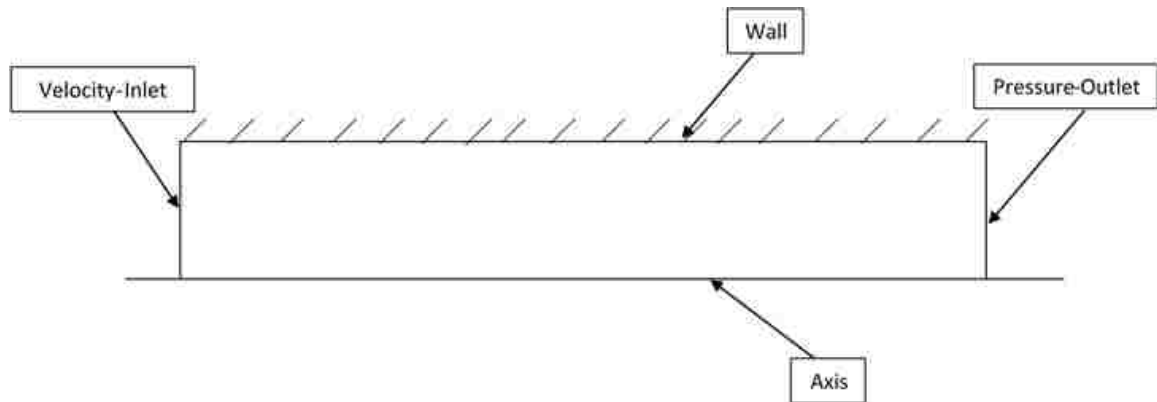
Figure 5.2. Diagram of Multiphase Microtube BCs.

iteratively to results in the correct inlet pressure, and the non-slip wall was run as adiabatic, radiative, and isothermal, in order to determine phenomena discussed later. This simulation used the coupled pressure-velocity scheme, but not the pseudo-transient solver, and second order discretizations. It was initialized via inlet velocity, temperature, and pressure, with the first 5% being patched with reactants and 1900K.

5.2. RESULTS

5.2.1. Multiphase Combustion Simulation. Unfortunately, a stable and accurate solution to the multi-mode thruster was not able to be obtained in ANSYS Fluent. In this section, the problems encountered, plots detailing issues, attempts to remedy, and the results of are presented. The following section attempts to draw conclusions from results obtained and problems encountered, namely the most probable causes of error, along with potential remedies that could be applied to future work.

Initial attempts to solve the simulation with the Phase-Coupled SIMPLE solver (the default solution method) resulted in divergence, and it was found that the Coupled solver combined with the Pseudo-Transient solver at a pseudo timestep of 1e-10 seconds, along with the Under-Relaxation Factors (URFs) all reduced as low as allowable, was required to bring the residuals to convergence. However, it was observed in this solution that

the property values, such as temperature and volume fraction, did not propagate beyond the initialized high temperature zone (20% of tube length), which does not make sense physically (Figures 5.3 and 5.4). Additionally, this solver setup only converged in a narrow

Figure 5.3. Temperature Contour of Pseudo-Transient Simulation Inlet.

Figure 5.4. $v_{f,l}$ Contour of Pseudo-Transient Simulation Inlet.

range of outlet pressures, which led to the conclusion that a better approximation for outlet static pressure was required.

A MATLAB code was written to calculate this new approximate p_e, in which a CV analysis was performed on an varying percentage of the thruster domain, labeled the combustion zone (CZ), with a known v, p, T, ρ, and v_f at the inlet side, and a known T, ρ,

and v_f at the outlet side. For this setup T_c, ρ calculated by the NASA CEA code, and a $v_{f,g}$ of 1 was used (Appendix C). These known values were used in the conservation equations for mass and momentum to determine the v_e and p_e of the combustion zone, followed by either Poiseuille or Fanno equations to calculate the exit values down the remaining length of the tube, depending on v_e. For all combustion zone lengths (0-100% of the tube), the flow was found to be not only subsonic, but incompressible post combustion, with a post combustion Mach number of 0.1045, which corresponds to a v of 101.3 m/s. Additionally, the pressure drop across the tube was plotted for all CZ lengths, with the largest drop observed to be approximately 7 psi from inlet to outlet, with the expected combustion zone length of 20% giving a drop of roughly 5.88 psi. Even keeping in mind the rough approximation this analysis provides, this small pressure drop leads to the outlet velocity being subsonic, and therefore a larger p_e was needed to better represent the flow.

This approximate p_e was used in conjunction with a UDF (see Appendix C) which simulates wall surface reactions for the multiphase case via limiting the reactions to the 5% of the thruster domain closest to the wall to attempt to solve the thruster. The combination of the complex modeling settings along with the UDF resulted in a segmentation fault due the large amount of memory required to run the simulation, so the less dense mesh of 67,500 cells was implemented in order to run the simulation (Figure 4.1). This setup converged without the need for the Pseudo-Transient solver, and allowed for larger URFs, which typically provides a more accurate solution. However, this new solution only converged after removing the reactions, even when initialized with a high temperature in the combustion zone and a large amount of gaseous product in the domain, both of which are recommended for kickstarting a steady-state combustion solution [5]. The wall condition was changed from radiative to adiabatic to determine if quenching via heat lost to the environment was hindering combustion, but this case also failed to show combustion. An isothermal case was then utilized in order to try and trigger combustion, but to no avail. Upon examination, it was determined that the residuals spend a period of time with large but steady residuals,

with the largest being continuity hovering around 1e+01 or larger. The $v_{f,g}$ at the outlet was calculated to vary between approx. 0.7-0.75, until a point where it quickly drops to almost zero. The majority of the residuals decrease to acceptable tolerances. An example case of this is shown in Figures 5.5 and 5.6:
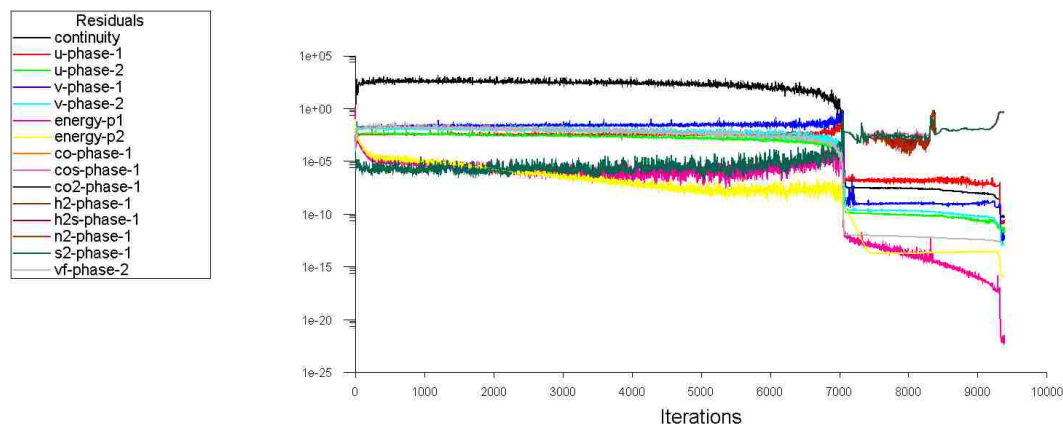
Figure 5.5. Typical Residual Plot of Heterogeneous Reaction Cases.
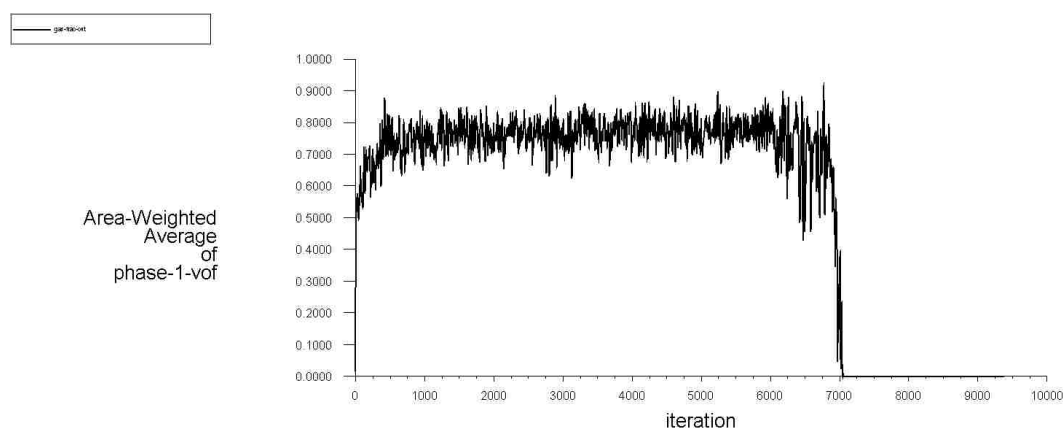
Figure 5.6. Typical $v_{f,g}$ at the Outlet for Heterogeneous Reaction Cases.

In these isothermal wall cases, the temperature of both the inlet and the wall was adjusted to see if it could trigger combustion. An inlet temperature of 500 K was used along with wall temperatures of 500, 600, 700, and 750 K producing roughly the same results in every case, specifically that the residuals failed to drop down low enough until Fluent removed the combustion process entirely.

5.2.2. Source Term Approximation. As the full multiphase combustion case did not converge successfully, an interim approximate solution was devised that would ideally provide some insight into the inner mechanisms of the thruster, until such a time that the propellant's experimental maturity had increased enough such that the errors of the full simulation could be fully diagnosed and corrected. This interim simulation took the results from the single phase combustion simulation (Section 4.2), and built upon it by "adding in" the mass and momentum missing due to the lack of liquid phase inlet properties via source terms applied to the Combustion Zone.

Similar to the process used to determine an approximate new p_e, the source terms were calculated using a CV analysis and the Conservation Equations for Mass, Momentum, and Energy. However, in this case, station 1 was taken to be the Single Phase Combustion properties, such as $\dot{m}$, p, u, and h, while station 2 was taken to be the post combustion values expected from the multiphase simulation, such as the larger $\dot{m}$, the h of products at the combustion temperature, etc. The discrepancy between these two stations was calculated via a MATLAB code (Appendix C), and labeled as the source term for that equation. For example, for the mass source term, the difference in mass flow rate between the Single Phase Combustion and Multiphase Combustion simulations were taken, and then divided by the volume of the CZ, taken to be the first 5% of the tube length, as the assumption of 20 % caused divergence in the inlet area of the thruster. These values were then input into a UDF (Appendix 1.4), which was used in the simulation to approximate the effects of the added mass and momentum from the liquid phase. The resulting simulation was then checked for accuracy via comparison to the NASA CEA results, as well as the Single Phase Combustion case, and source term values were iteratively adjusted as necessary to achieve expected values for y_j, property data, T_c, and inlet pressure p_i. The need to adjust for inlet pressure was borne out of the way Fluent treats pressure data at the boundaries, discussed in Section 5.3. This Source Term Simulation was executed similar to the Single Phase combustion case, in that an adiabatic solution was first obtained to examine the combustion

temperature and property data, followed by a radiative wall solution, to better examine the real flow solution. These simulations were run using the 100,000 element mesh (Figure 5.1), with the coupled solver, and second order spatial discretization.

The results for this Source Term Approximation Sim are displayed in Tables 5.1 and 5.2. The %Diff shown in Table 5.1 from the adiabatic setup shows a similar level of tolerances as the Single Phase Combustion case, which is what determined it to be accurate enough to perform a radiative case.

Table 5.1. CEA-Source Term Approx. Property Comparison.

Property	NASA CEA	FLUENT	%Diff
MW (kg/kmol)	20.8190	20.8243	0.0255
T_c (K)	1903.34	1911.57	0.4325
Cp (kJ/kg-K)	2.1709	2.0243	6.7526
γ	1.2341	1.2457	0.9394
u^* (m/s)	968.5	975.1	0.6769

The outlet mass fractions for the radiative case are in a similar scenario in terms of %Diff, with the exception of the outlier value for H_2O, 0.1276%, which is still considered an excellent value. Additionally, T_e, M_e, $\dot{m}$, and P_i were calculated, shown in Table 5.3. It can be observed that there is very good agreement with p_i, but only rough agreement in $\dot{m}_e$, and a fairly large disparity in M_e. The reasoning for these is discussed in Section 5.3.2. Lastly, the temperature profiles of the wall, axis, and area-averaged slices were plotted against each other, shown in Figure 5.7. This figure depicts a much more constant temperature profile than the Single Phase Combustion case, along with a higher peak temperature of 2769.37 K, however both are easily explained. As there is more mass in the tube due to the mass source term (more specifically, 96% of the mass at the outlet was added via the source term), the heat does not dissipate as easily, resulting in a higher temperature at the outlet. For the peak temperature, this is considered to be an artificially high temperature resulting from the compounding error of both a one-step Arrhenius model (the cause of the

Table 5.2. Source Term Approx. Outlet Mass Fraction Comparison.

Species	Theoretical	FLUENT	%Diff
Prop	0	5e-4	
CO	0.2925	0.2924	0.0264
COS	0.0037	0.0037	0.0238
CO_2	0.1486	0.1486	0.0262
H_2	0.0211	0.0211	0.0327
H_2O	0.2568	0.2565	0.1276
H_2S	0.0499	0.0499	0.0256
N_2	0.2207	0.2206	0.0266
S_2	0.0067	0.0067	0.0387

Table 5.3. Source Term Approx. Outlet Properties.

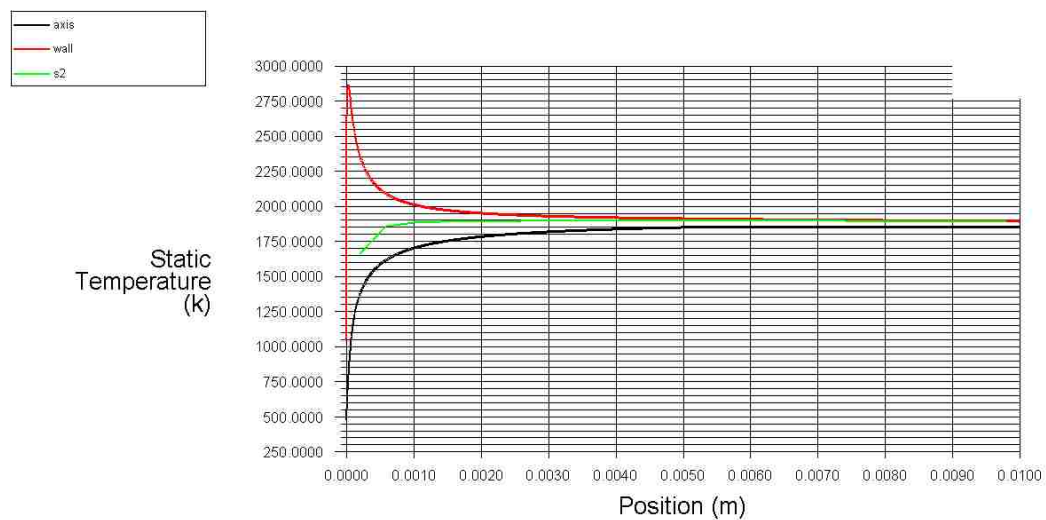| Property	Expected	FLUENT	%Diff
T_e (K)		1795.73	
M_e	0.1045	0.0895	14.3536
$\dot{m}_e$ (kg/s)	2.13e-05	1.97e-05	7.5475
P_i (Pa)	1378951	1378103	0.0615

Figure 5.7. Temperature Profile of Wall, Centerline, and Average in Source Radiative Wall Case vs. Axial Position (m).

high temperature in the Single Phase Combustion case), and the energy source term being added in at the same location. Therefore, this large of a temp is not expected to be seen on an experimental setup, and should decrease/dissipate entirely once a more comprehensive model is converged. p_i was tracked as well to determine a rough accuracy for the pressure drop calculated in the MATLAB code used in Section 5.2, in which p_o was adjusted to the value required to achieve approximately the known p_i. For this simulation, the %Diff for p_i was determined to be 0.0615%, and the %Difference for the p_e between this and the approximation code was 0.1613%.

For comparison, contour plots of temperature, velocity, and propellant mass fraction in the inlet region (Figures 5.8, 5.9, and 5.10) covering roughly the same area as the single phase contours have been generated and included for the Source Term Approximation case.

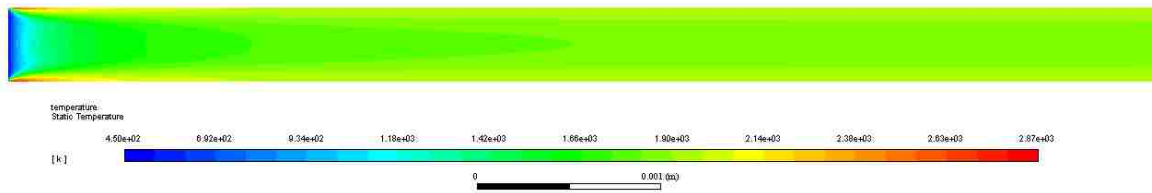Figure 5.8. Inlet-Focused Temperature Contour for Source Term Approximation Case.

Additionally, plots for the radial profiles of propellant mass fraction and nondimensionalized velocity, matching the ones for single phase (Figures 4.9 and 4.10). An analysis comparing the two graphs is performed in the following section.

Figure 5.9. Inlet-Focused Velocity Contour for Source Term Approximation Case.
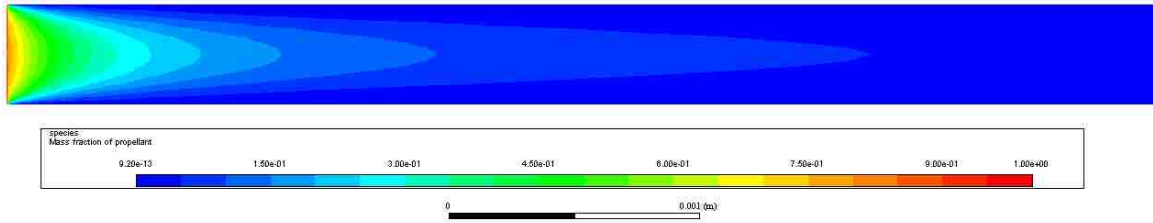
Figure 5.10. Inlet-Focused Propellant Mass Fraction Contour for Source Term Approximation Case.
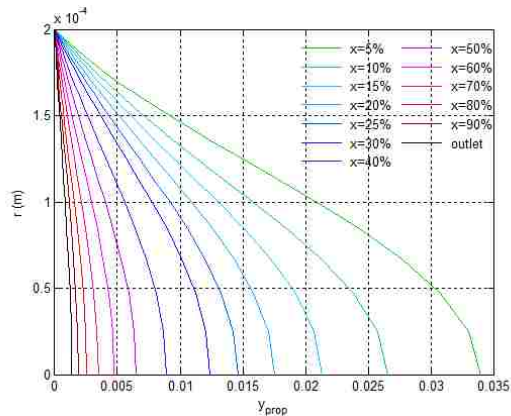

Figure 5.11. Radial Profiles of Propellant Mass Fraction for Source Term Case.
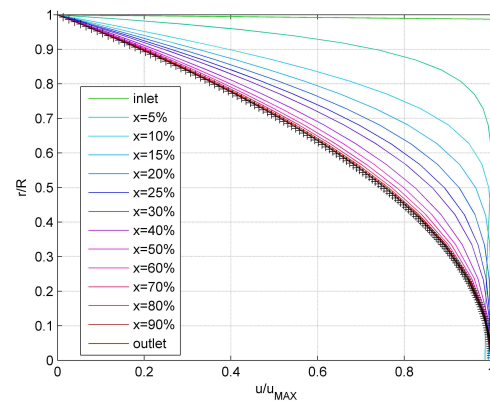
Figure 5.12. Radial Profiles of Nondimensionalized Flow Velocity for Source Term Case.

5.3. DISCUSSION

5.3.1. Multiphase Combustion Simulation. From analysis of the attempted multiphase combustion simulations and their results, it was determined that the most probable cause of error is related to either the reaction mechanism or the boundary conditions.

- Reaction Mechanism: While the one-step Arrhenius reaction mechanism was successful in the single-phase combustion case in terms of T_c, product gas properties, and outlet species distribution, the addition of multiphasic effects could very well require a more complicated reaction mechanism in order to capture the physics of the phase change (For example, injected liquid fuel typically evaporates before decomposing/combusting into products). A similar process for the novel propellant before catalytic

decomposition could very well be taking place for one or both components of the mixture. Another possibility would be that the decomposition of one part occurs first, which could provide the heat release to ignite the second component, and therefore bring the reaction into a self sustaining state. The current one-step mechanism ignores such phenomena. Unfortunately, the propellant has not yet reached a maturity that would provide data on such a process via a two or more step mechanism, so only the one step is available.

The only concrete solution to this problem would be either to wait until the property data necessary to improve the simulation is available, or to execute methods to determine a multi-step reduced mechanism. The simplest multi-step mechanism would most likely consist of a process that governs the phase change, whether it uses some form of vaporization or reaction, followed by the already determined one-step mechanism, most likely with slightly altered rate constants. Such a mechanism would be much better suited to capture the transfer of momentum/energy from one phase to the other and thus provide better convergence.

- Boundary Conditions: As there is little experimental data to compare the simulation to (the closest to a successful steady state is in Berg and Rovey [20], where the combusting test fire removed the thruster from the housing, preventing data from being obtained), determination of correct boundary conditions such as outlet pressure and steady state wall temperature for a complex case such as this is a daunting task, especially since the simulation has been observed to be very sensitive to small changes in the boundary conditions. This sensitivity removes the ability to adjust the outlet pressure based on converged results, a guess-and-check style method for estimated values, which is a possibility for other cases, due to how Fluent treats some boundary conditions. Specifically, when using a pressure outlet BC, Fluent treats the value input at the outlet as a hard BC (the exact value is forced in the solution) and the defined inlet pressure as a soft BC (the provided value is treated as an initial guess)

for subsonic flow, and vice versa for supersonic flow. This treatment, and the belief that the flow at the outlet would be roughly sonic and should adopt the hard inlet behavior, is what initially led to the development of the model before a successful steady state test was performed, as Fluent was expected to deviate the outlet pressure to a better value. Additionally, knowledge of boundary conditions determines the best way to initialize the simulation, which could be the difference between convergence and divergence for a sensitive simulation such as this one.

Obviously, the solution to this issue would be to obtain more testing data from which more accurate boundary condition data can be determined and used. From there, the simulation could be updated to conclude if the boundary conditions were indeed the cause of divergence, or if it was another factor. Between the two proposed error sources, this solution is the simplest to implement, as well as the more probable of the two, due to the ubiquity of one-step reaction mechanisms. It is worth noting that the cases which failed to combust correlate in that fact to the experimental test fire data in Berg and Rovey [20].

A possible next step, as well as an interim solution for the increased maturity of the propellant, would be to model the same setup for a surrogate multi-step mechanism, using a similar, but more characterized propellant. This would involve essentially determining a similar propellant via a metric that compares them (e.g. Isp, molecular composition, or blend components, such as just [Emim][EtSO$_4$] or just HAN), and determining a domain which appropriately captures its combustion, and applying this more common mechanism and boundary conditions. While the determination of boundary conditions for such a case might require some experimentation, the process of using a surrogate mechanism would provide a large step toward determining the probability of the error being due to the one-step mechanism, as if it works for another system, then it should also work for the novel

monopropellant. While the results determined from such an analysis would be approximate in respect to a comprehensive multiphase solution, the insights provided would still be valuable in terms of error reduction towards this comprehensive simulation.

5.3.2. Source Term Approximation. While the results from the Source Term simulations are approximate at best, they can still provide some useful information. Firstly, it can be observed that the outlet temperature for this case was 777.85 K higher than the outlet temperature observed in the Single Phase Combustion case. As previously mentioned, this makes sense physically, as the larger amount of mass would take more time (or in this case, pipe length) to cool to the same temperature as the single phase case. However, due to the approximate nature of the simulation, it is reasonable to expect the actual temperature measured to fall somewhere either in the range between these two numbers, or near this larger number, as the full multiphasic effects may require more energy to change phase, or more heat may be lost to the environment, or a similar phenomenon.

Another point of note is the much larger amount of propellant in the outlet, compared to the Single Phase Combustion case (5e-04 v. 3e-17). This is most likely due to the added mass taking a portion of the heat from combustion to heat itself up to the same temperature as the surroundings, which in turn leaves less heat or the decomposition of the propellant. While this phenomenon is not expected to carry over to a more comprehensive sim, it is also worth noting that this still results in 98.5% of the propellant combusting in the CZ.

It can be observed from Table 5.3 that there exists some significant errors for both M_e and $\dot{m}_e$. The %Diff for M_e is something that can be taken loosely, as the expected value was taken from the approximate CV analysis performed to improve the Multiphase Combustion case, and is therefore only expected to be roughly the same as the actual outlet Mach Number. Because of this, the important thing to note from these two numbers is that they are both firmly subsonic, which lends even more credence to the actual flow not reaching the sonic condition at the outlet. The error in $\dot{m}_e$ is due to a difference in the calculation of $\dot{m}$ between the two sources, in which the reference number is based on the

volumetric flow rate in Berg and Rovey [20], multiplied by the density ρ of the propellant, and the simulation value being calculated from the average velocity of the expected range experienced by the testing setup, and multiplied by the density determined from Eq. 3.7, and the cross-sectional area of the tube. when the latter method is applied to the expected value, the error reduces to 0.32%, which is well within acceptable tolerance. Lastly, the %Diff accuracy of the p_i calculations provide some credibility for the p_e calculated for use in the comprehensive Multiphase Combustion simulation.

When viewing Figures 4.6-4.8 and Figures 5.8-5.10 side by side, the most striking difference is in how the flow variables develop. For temperature, the roughly conical shape of the inlet temperature region is replaced by a much flatter transition, which is due in part to the application of the source terms. However, the high temperature zone at the onset of combustion is quickly cooled by the radiative walls. The source term velocity contour develops much more slowly than its counterpart, which is caused by the additional mass, as this raises the velocity of the flow, which in turn lengthens the entry length corridor. This can be further observed in Figure 5.12, in which the flow approaches the Poiseuille Line, denoted by the + symbols, but doesn't completely reach it, as opposed to the single phase case (Figure 4.10, which achieves this developed state by the 20% mark. This suggests that the flow isn't fully developed, which matches with the propellant mass fraction profiles in Figure 5.11, as well as from a physical standpoint, as discussed earlier. The conclusions drawn from these plots also highlights the approximative nature of the source term simulation, as several of the properties were calculated assuming developed flow.

6. CONCLUSIONS

In order to obtain more detailed data on the catalytic combustion of a novel mono-propellant in a microtube, current experimental data was taken and used to develop a CFD model in ANSYS Fluent. All aspects of the model used were explained and benchmark cases were provided to prove accuracy of models. The previously elucidated ([15]) one-step reaction equation was shown to not fit within Fluent's mass tolerance, so products were recalculated, and several trace species were identified to close the gap. The new reaction mechanism was confirmed to compare to previous product property values, and was shown to work in Fluent via a single-phase case, with all properties within acceptable tolerances except for c_p, whose error was determined to be caused by curve fit constants. This case showed a much smaller pressure drop than expected, as well as a highly subsonic outlet, implying a large contribution to the flow from multiphasic effects.

The full multiphase combustion simulation was found to experience convergence issues, which led to an adjustment in case setup to determine the cause. The new BCs used a smaller pressure drop, and convergence was found only upon removal of combustion from the flow. From analysis, the most likely cause of error was hypothesized to be numerical approximations to the unknown steady state boundary condition in the monopropellant's experiment. It was determined that the multiphasic effects could be approximated through source terms applied to the single phase case, and so such a simulation was executed. This simulation showed a larger pressure drop, outlet temperature, and outlet velocity than the single phase case, however the drop was still much smaller than expected, and the velocity was firmly subsonic ($M_e = 0.0895$), which further supported the hypothesis of a subsonic outlet. Given that the existing simulations cannot match all the desired quantities in the experiments, additional simulations with better designed boundary conditions and numerical models are necessary for them to fully explain the experiments.

APPENDIX A.

BENCHMARK CASES

As models are, in essence, just equations being solved from the data given to them, and therefore can come to a solution that is ultimately incorrect and not reflective of reality due to incorrect inputs, it is common practice to show that a model setup is accurate by comparing it to an analytical solution or a benchmark case, which is a situation with a well known/well defined solution. Typically benchmark cases focus on only one aspect of a flow, so in this section, each constituent piece of the overall simulation is compared to one of these benchmark cases, in order to prove accuracy in the setup of said simulation, thus reducing sources of error. Each aspect will explain what the benchmark case it is being compared to is, as well as show the results that prove the setup accurate.

0.1. COLD, SINGLE PHASE FLUID FLOW

0.1.1. Incompressible Laminar Liquid Flow. Assuming that the flow is driven by the pressure difference between the inlet and outlet, there exists an exact solution to the Navier-Stokes Equations for an incompressible laminar fluid flowing in a duct with stationary walls, named Hagen-Poiseuille flow. The viscous boundary layers from the walls of the duct gradually extend from the walls until they connect in the center, at which the viscous effects extend to the entirety of the tube. This separates the duct into two distinct regions: the hydrodynamic entrance region and the fully developed region. In this fully developed region, [42] proves that the fluid develops a constant parabolic velocity profile, calculated by Eq. 1

$$v_{nondim} = 1 - r_{nondim}^2 \tag{1}$$

where $v_{nondim} = v/(2v_m)$ and $r_{nondim} = r/R$. The distance required for the flow to fully develop into this condition has been best approximated as

$$L_e \approx 0.06 Red \tag{2}$$

where *Re* is the Reynolds Number, a nondimensional ratio of inertial to viscous forces, at the inlet [42].

To model this in Fluent, a simulation was made of water in a 200 micron diameter pipe, with an inlet velocity of 1 m/s at STP. These conditions resulted in a *Re* of 13.5, and therefore an L_e of approx. 2.4 mm. This was used to calculate an approximate exit pressure p_e using Eq. 3

$$v = \frac{R^2}{16\mu L} \frac{p_i^2 - p_e^2}{p_e};$$

(3)

which was iteratively solved, giving an exit pressure of 98945 Pa. The resulting outlet velocity profile of the model was nondimensionalized and plotted against the Poiseuille Distribution in Fig 1. It can be observed that the lines are essentially the same, which is
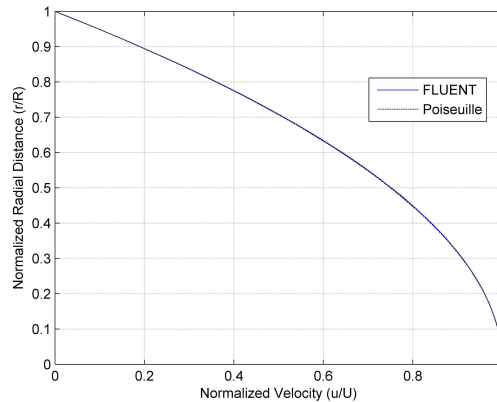

Figure 1. Developed Velocity Profile Comparison for Poiseuille Flow and Fluent Simulation.

reflected in the maximum error between them of 0.51%.

0.1.2. Compressible Laminar Gas Flow. For compressible internal flows, exact solutions, such as Hagen-Poiseuille for incompressible flow, do not exist. However, there are methods that give good approximations from basing their equations in incompressible flows and adding correction factors to fit to experimental data, and others making reasonable simplifications. One such case is Fanno Flow, in which internal constant area Quasi-1D

adiabatic inviscid flow is taken, and then only viscous effects are counted. Under these conditions, the flow can be observed to always move towards a sonic state ($M = 1$) regardless of inlet conditions, which is known as viscous choking.

In order to compare simulation values to this solution, which assumes a constant velocity profile, it is convenient to use a mean velocity for comparison (Eq. 4):

$$v_m = \frac{1}{A_c} \int v \, dA_c \tag{4}$$

Additionally, the compressible flow equations are much simpler in terms of Mach Number M, or the flow speed relative to the local speed of sound a:

$$M = \frac{v}{a} = \frac{v}{\sqrt{\gamma \frac{\mathcal{R}}{MW} T}} \tag{5}$$

where $\gamma = c_p/c_v$ is the Ratio of Specific Heats (For air, $\gamma = 1.4$). For Fanno Flow, the exit conditions of a duct are found via derivations of the mass, momentum, and energy conservation equations, using the assumptions of a perfect, calorically perfect gas (CPG). The final equations are presented as a ratio to the sonic case ($M = 1$), which is used as an intermediary to calculate property ratios between the two points [43]:

$$\frac{p}{p^*} = \frac{1}{M} \left[\frac{\gamma + 1}{2 + (\gamma + 1)M^2} \right]^{1/2} \tag{6a}$$

$$\frac{\rho}{\rho^*} = \frac{1}{M} \left[\frac{2 + (\gamma + 1)M^2}{\gamma + 1} \right]^{1/2} \tag{6b}$$

$$\frac{T}{T^*} = \frac{\gamma + 1}{2 + (\gamma + 1)M^2} \tag{6c}$$

$$\frac{p_o}{p_o^*} = \frac{1}{M} \left[\frac{2 + (\gamma + 1)M^2}{\gamma + 1} \right]^{(\gamma+1)/[2(\gamma-1)]} \tag{6d}$$

The momentum equation can also be manipulated to give the location of the flow becoming sonic:

$$\frac{f_m L^*}{d} = \frac{1 - M^2}{\gamma M^2} + \frac{\gamma + 1}{2\gamma} ln\left[\frac{(\gamma + 1)M^2}{2 + (\gamma - 1)M^2}\right] \tag{7}$$

where L^* is the sonic length, and f_m is the average friction factor, which is calculated using a Moody Chart and Eq. 8:

$$f_m = \frac{1}{L^*}\int_0^{L^*} f\,dx, \tag{8a}$$

$$f \approx \frac{f_{inc}}{\sqrt{1 + \frac{\gamma-1}{2}r_{rec}M^2}} \tag{8b}$$

where f_{inc} is the incompressible friction factor obtained from a Moody Chart, r_{rec} is a recovery factor ($r_{rec} = \sqrt{Pr} \approx 0.85$ for laminar flow), and f is the corrected factor for compressible flow. As the f distribution is not necessarily known throughout the tube, a common approximation is to use the inlet f_m throughout the tube.

The solution procedure for a Fanno Flow problem utilizes Eq. 7 and a 'virtual length' (Figure 2) in order to determine the exit conditions [43]. Due to the Fanno Flow Equations all being referenced to the sonic conditions, this virtual length is an imaginary extension of the duct beyond the exit to this sonic length. Denoting this new length addition as L_2^*, the sonic length for the inlet (L_1^*) can be seen to be the summation of the actual pipe and this virtual length, i.e. $L_1^* + L = L_2^*$. Noting that f_m and d are both constant and known, this can be manipulated:

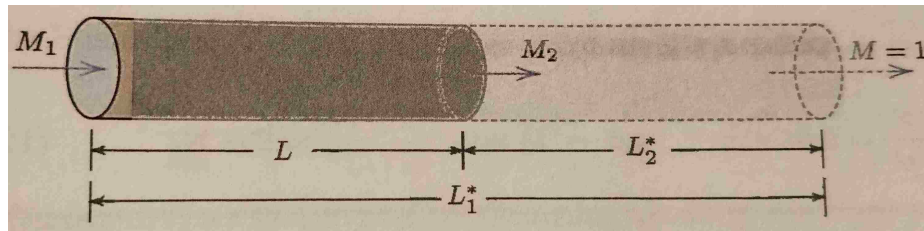$$\frac{f_m L_2^*}{d} = \frac{f_m L_1^*}{d} - \frac{f_m L}{d} \tag{9}$$

Figure 2. Virtual Length [43].

where the resulting $\frac{f_m L_2^*}{d}$ term can then be used to calculate the inlet M of the virtual length, which is also the exit M of the actual pipe. As Eq. 7 cannot be solved analytically, this is done either numerically, or via tabulated values and interpolation. Once M_e is calculated, it is a simple matter of combining the ratios calculated in Eq. 6 to get the exit properties as a function of entrance properties [43].

For a benchmark simulation to compare to Fanno Flow, two simulations were designed of air in a duct with a diameter of 200 microns and a length of 10 cm. The air enters at 100 kPa and 293 K, with one case having an inlet speed of 0.088 Mach, and the second at 0.091 Mach. From Eqs. 6 - 7 the analytical approximate exit conditions were calculated for both cases. It was determined that a correct simulation will have not only the correct values for the variables, but also an outlet velocity profile similar to the Poiseuille Distribution, as the flow is pressure driven, but compressibility causes a lengthening of the entrance region. These results can be observed in Figure 3, and Tables 1 - 2.
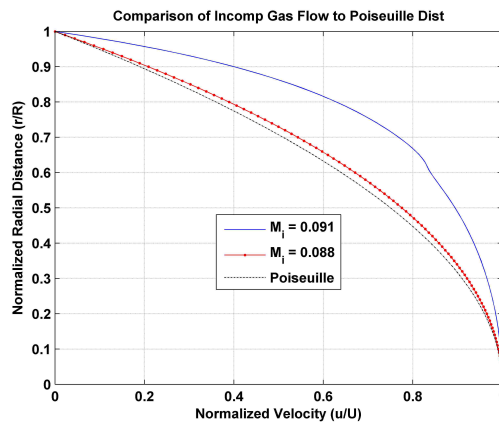

Figure 3. Comparison of Outlet Velocity Profiles to Poiseuille Distribution.

Table 1. Result Data for $M_i = 0.088$ Case.

Property	Analytical Value	Experimental Value	% Error
M_e	0.2417	0.2710	12.11%
P_e (Pa)	32254.93	32732	1.48%
T_e (K)	289.21	287.45	0.61%
$P_{o,e}(Pa)$	34702.83	35407.78	0.99%

Table 2. Result Data for $M_i = 0.091$ Case.

Property	Analytical Value	Experimental Value	% Error
M_e	0.8072	0.8116	0.54%
P_e (Pa)	10549	10011.41	5.10%
T_e (K)	259.32	248.82	4.05%
$P_{o,e}$ (Pa)	16278	17425.12	7.05%

From analysis of Figure 3 it can be observed that while the slower simulation outlet profile correlates very well with the Poiseuille distribution, the faster sim has only a roughly similar shape. The main cause of this is compressibility effects. For the slower sim, while the highest speed experienced in the outlet is $M \approx 0.52$, which is well in the compressible regime, the average Mach is only ≈ 0.27, so the majority of the flow experiences only minor compressibility, and therefore minor deviation from the incompressible Poiseuille distribution. Conversely, the fast sim has an average exit Mach of ≈ 0.81, and a local top speed of ≈ 1.22 Mach, which is both highly compressible and locally supersonic. At these speeds, the compressibility effects are much greater, and therefore cause a much larger deviation from incompressible profiles.

The high speeds experienced at the fast simulation outlet may initially cause concerns, as one of the rules of Fanno Flow is that the flow always approaches the sonic condition, but never crosses it. However, Fanno Flow typically deals with uniform velocity profiles, and as the mean value of the outlet has not violated this rule, it was determined to be allowable. Additionally, the short period in the velocity profile where the gradient becomes much sharper corresponds with where the flow locally becomes supersonic, which lends itself to the idea that this is a form of flow discontinuity.

From Tables 1 and 2, it can be seen that the values obtained from the simulation match quite well with the calculated Fanno values, with the exception of M_e on the slower simulation, which is much higher than the rest at 12.11%. The exact cause of this was not

determined, however the staggering difference compared to the rest of the values suggests some sort of minor calculation error in either the analytical or the Fluent calculation, most likely related to the low amount of compressibility in the flow.

0.1.3. Heated Walls via Imposed Temperature or Heat Flux. When flow enters a tube in which the walls are heated or cooled relative to the flow, there develops in the flow a thermal boundary layer, and thus a thermal entrance region, analogous to the hydrodynamic entrance region experienced in viscous pipe flows. In laminar flow, this thermal entrance region length is expressed as

$$L_{e,th} \approx 0.05 RePrd \tag{10}$$

It is worth noting that the Prandtl Number, Pr, is the major driver in whether the fluid develops hydrodynamically or thermally first [21].

In order to analyze this phenomenon, Bergman et al. [21] defines a mass-averaged mean temperature T_m

$$T_m = \frac{\int_{A_c} \rho u c_p T \, dA_c}{\dot{m} c_p} \tag{11}$$

with which it nondimensionalizes the temperature of the fluid in a manner that allows for a constant developed profile, shown in Eq. 12:

$$\theta = \frac{T_w(x) - T(r, x)}{T_w(x) - T_m(x)} \tag{12}$$

While the local value of T will continue to change with x, this nondimensional temperature θ will become a function of radius only, which denotes the flow as fully developed.

By applying the conservative form of the energy equation to a differential element in the fully developed region of the fluid, it can be shown that

$$v_x \frac{dT}{dx} = \frac{\alpha}{r} \frac{\partial}{\partial r} \left(r \frac{\partial T}{\partial r} \right) \tag{13}$$

Combining Eq. 13 with the boundary conditions for either uniform q_w or T_w, this equation can be used to determine properties of the thermally developed flow.

0.1.3.1. Uniform surface heat flux. In the case of a uniform q_w, and recognizing that in the fully developed region of the flow, the heat transfer coefficient h_Q is constant, it can be derived from Newton's Law of Cooling that

$$\left.\frac{dT_w}{dx}\right|_{fd,th} = \left.\frac{dT_m}{dx}\right|_{fd,th} \tag{14}$$

and by considering that for fully developed flows, θ is constant, we can calculate that

$$\left.\frac{dT}{dx}\right|_{fd,th} = \left.\frac{dT_m}{dx}\right|_{fd,th} \tag{15}$$

Using Eqs. 14 and 1, we can reduce the energy equation 13 to

$$\frac{1}{r}\frac{\partial}{\partial r}\left(r\frac{\partial T}{\partial r}\right) = \frac{2v_m}{\alpha}\left(\frac{dT_m}{dx}\right)\left[1 - (r_{nondim})^2\right] \tag{16}$$

where $T_m(x)$ varies linearly and $(2v_m/\alpha)(dT_m/dx)$ is a constant. Through separation of variables and integration, a radial temperature distribution was obtained (Eq. 17):

$$T(r,x) = \frac{2v_m}{\alpha}\left(\frac{dT_m}{dx}\right)\left[\frac{r^2}{4} - \frac{r^4}{16R^2}\right] + C_1 ln(r) + C_2 \tag{17}$$

where, utilizing the boundary conditions, it was determined that $C_1 = 0$, as the temperature must remain finite at $r = 0$, and because $T(R,x) = T_w(x)$, C_2 became

$$C_2 = T_w(x) - \frac{2v_m}{\alpha}\left(\frac{dT_m}{dx}\right)\left(\frac{3R^2}{16}\right) \tag{18}$$

and the developed temperature profile was found to be

$$T(r,x) = T_w(x) - \frac{v_m R^2}{8\alpha}\left(\frac{dT_m}{dx}\right)\left[3 - r_{nondim}^2 + r_{nondim}^4\right] \tag{19}$$

Using this result in conjunction with Eqs. 11 and 1, the integration in r was performed, and a solution for mean temperature was calculated:

$$T_m(x) = T_w(x) - \frac{11}{48}\left(\frac{v_m R^2}{\alpha}\right)\left(\frac{dT_m}{dx}\right) \tag{20}$$

From here, the text combines Eq. 20 with the energy balance on a differential duct element (Eq. 21a) to determine the final result:

$$dq_{conv} = \dot{m}c_p dT_m \tag{21a}$$

where q_{conv} is the convective heat transfer. Using that for said differential element, $dq_{conv} = q_w P dx$ where P is the perimeter of the duct, an equation for dT_m/dx is found (Eq. 21b):

$$\frac{dT_m}{dx} = \frac{q_w P}{\dot{m}c_p} = \frac{P}{\dot{m}c_p}h_Q(T_w - T_m) \tag{21b}$$

Finally, using that for circular ducts, $P = \pi d$ and $\dot{m} = \rho v_m(\pi d^2/4)$, a solution for Nusselt Number is found:

$$T_m(x) - T_w(x) = -\frac{11}{48}\frac{q_w d}{k} \Rightarrow h_Q = \frac{48}{11}\left(\frac{k}{d}\right) \tag{21c}$$

$$Nu = \frac{h_Q d}{k} = 4.36, \quad q_w = constant \tag{21d}$$

Therefore, in laminar, fully developed flow, there is a constant Nu of 4.36 [21].

In order to determine a nondimensionalized temperature profile for the developed flow, it is a simple matter of rearranging Eqs. 19 and 20 to put the temperature terms on one side, and then dividing the first by the second:

$$\frac{T_w(x) - T(r,x)}{T_w(x) - T_m(x)} = \theta(r) = \frac{Nu}{8}(3 - 4r_{nonidm}^2 + r_{nonidm}^4) \tag{22}$$

From these results, it was determined that the way to verify a simulation of this type would be to compare the nondimensional temperature profile at the outlet, as well as the Nusselt Number along the centerline, to ensure that the flow developed near the expected axial location.

To model this in Fluent, a simulation was designed for a 200 micron diameter pipe filled with water vapor, with an uniform inlet velocity of 25 m/s, inlet temperature of 400 K, outlet pressure of 1 atm, and a constant wall heat flux of 10,000 W/m^2. These conditions resulted in a *Re* of 127.288, and thus an $L_{e,th}$ of 1.529 mm. Once completed, the Area-averaged Nusselt number was calculatedto determine where the flow fully developed via the Laminar Sieder-Tate Correlation:

$$Nu_x = 1.86(RePr)^{1/3}\left(\frac{d}{x}\right)^{1/3}\left(\frac{\mu}{\mu_w}\right)^{0.14} \tag{23}$$

As this equation is only valid in the thermal entry region, it was determined that when the result matched the expected constant Nu value of 4.36, the flow was considered fully developed (Figure 4). Additionally, the outlet temperature profile was nondimensionalized and plotted against the expected profile for accuracy (Figure 5) It can be observed from Figures 4 and 5 that the flow is fully developed at the outlet, and becomes such at approx.
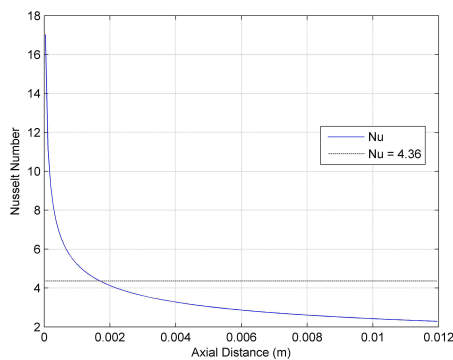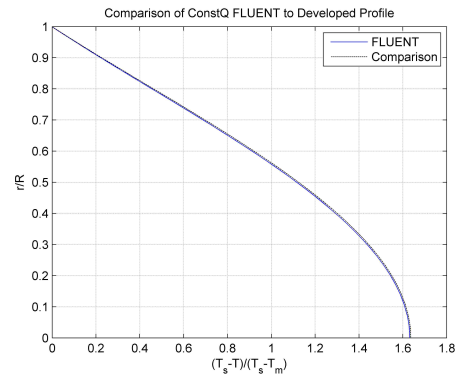

Figure 4. Nu Dist for q_w = constant.

Figure 5. Comparison of Outlet Temp. Profile to Expected Solution.

1.719 mm. While this value corresponds to a larger error than desired (specifically, 12.483 %), the fact that this Sieder-Tate Correlation is approximate equation means that this error is still within reason.

0.1.3.2. Uniform surface temperature. In a similar fashion to Eq. 14, for the case of a constant wall temperature T_w, we arrive at

$$\left.\frac{\partial T}{\partial x}\right|_{fd,th} = \frac{(T_w - T)}{(T_w - T_m)}\left.\frac{dT_m}{dx}\right|_{fd,th} \tag{24}$$

Using this result, along with Eq. 1, the energy equation becomes

$$\frac{1}{r}\frac{\partial}{\partial r}\left(r\frac{\partial T}{\partial r}\right) = \frac{2v_m}{\alpha}\left(\frac{dT_m}{dx}\right)\left[1 - r_{nondim}^2\right]\frac{T_w - T}{T_w - T_m} \tag{25}$$

This equation cannot be solved analytically, but can through an iterative procedure over approximations on the temperature profile. This makes the temperature profile for the Constant T_w case unable to be simply described and nondimensionalized, as it is with the constant q_w case, but the Nusselt Number does resolve to a constant 3.66 [21].

The Fluent model for this case was the same as the Uniform Heat Flux case, with the wall boundary condition changed to be a constant 600K. Eq. 23 was then used to calculate the Nusselt Number along the centerline to determine that the flow was fully developed: This case had a larger error in $L_{e,th}$ than the Heat Flux case, with a 35.62% disparity between the two values. It was determined that the main cause of this disparity was due to the lower heat flux being transferred into the flow as it progressed down the tube from the decreasing temperature difference between the wall and bulk fluid, which slowed the development.
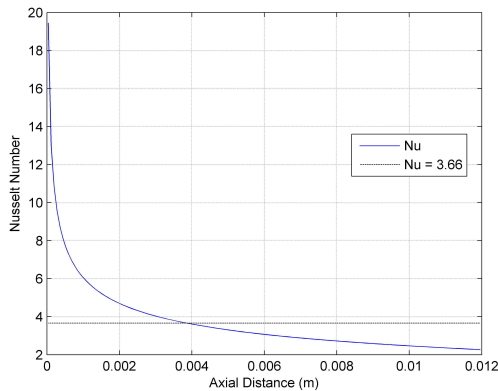
Figure 6. Area-Averaged Nu for T_w = constant.

0.2. GAS PHASE REACTION KINETICS

0.2.1. Volumetric Reactions. For modeling chemical reactions, a typical benchmark consists of a fairly simple geometry with a well understood reaction. A good example of this would be the reaction between methane and air, which has numerous mechanisms such as one-step, two-step, reduced mechanisms of approx. 30 species, the full GRI Mech 3.0 containing 53 species and 325 reactions, and many others in between, containing varying numbers of species and reactions.

The simulation used for a benchmark of this simulation aspect is lean premixed methane-air combustion in a conical chamber (Figure 7), using the Finite-Rate Chemistry model [31]. This particular simulation was found on the Mr. CFD website [9], and utilizes a 5-step global mechanism (detailed in Table 1) which was developed by Nicol [34] to "observe methane oxidation and NO formation... for lean, premixed combustion applications" [31]. This particular mechanism is valid for a pressure of 1 *atm*, inlet temperature of 650 *K*, and an equivalence ratio ϕ_{eq} of 0.45-0.70.

The simulation of this mechanism used an inlet velocity of 60 *m/s*, and an ϕ_{eq} of 0.6, which falls into the acceptable range. The method used was the Finite-Rate/Eddy Dissipation model, in conjunction with the k-ϵ turbulence model. It was first solved as a cold flow, in order to establish the flow field, for 200 iterations, and then the reactions were turned on
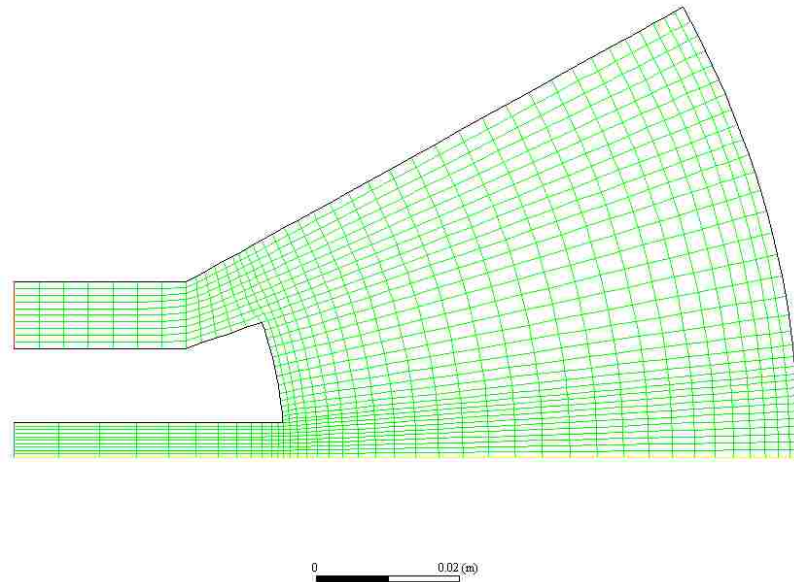
Figure 7. Meshed Domain of Conical Chamber.

in order to model the combustion. Once this had converged, contour plots of parameters such as velocity, temperature, and species mass fractions were generated to compare for accuracy, of which several are shown below, with additional figures in Appendix A (Figures 1 - 4:
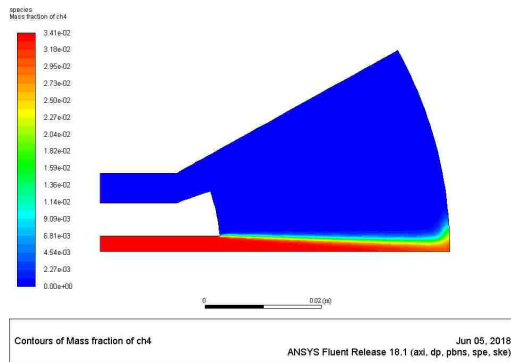

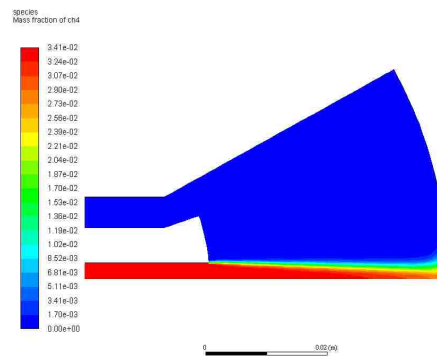Figure 8. CH_4 Contour from Generated Sim.

Figure 9. Provided CH_4 Contour [9].

From comparison of these figures, it can be observed that the generated simulation matches up very well with the provided comparison data. From this, it can be concluded that the simulation is resolved accurately.
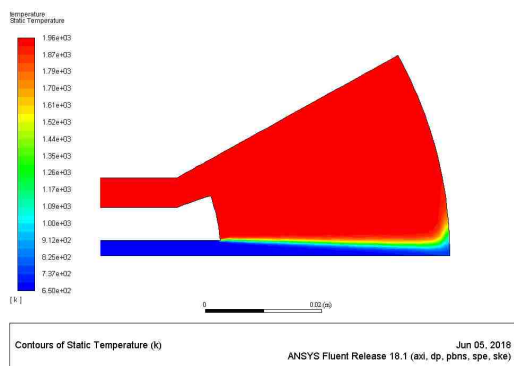
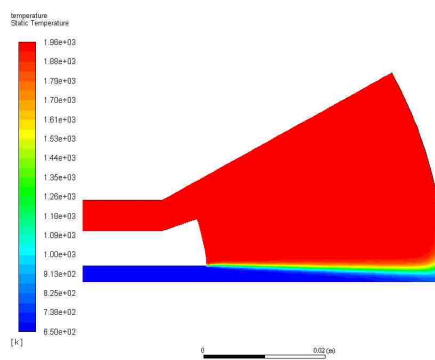Figure 10. Temperature Contour from Generated Sim.

Figure 11. Provided Temperature Contour [9].

0.2.2. Surface Catalyst Reactions. Due to the complexity of surface catalyst chemistry, a typical benchmark case is not typically something that can be readily obtained. Because of this, a well documented simulation over catalytic combustion which can be reproduced and compared to for accuracy was used instead, obtained from the Mr CFD Website [9]. The obtained simulation consisted of a gaseous mixture of methane, hydrogen, and air entering a cylindrical tube, wherein they catalytically combust with the wall, which is modeled to be heated and lined with platinum as a catalyst material [30].

In this simulation, A cylindrical pipe with a length of 6 cm and a diameter of 1.8 mm, with the aluminum walls lined with a platinum catalyst from 0.5 cm to 5.5 cm and heated to 1290 K, is treated to a mixture of Methane, Hydrogen, and Air entering the inlet at 0.8 m/s, 1 atm, and 300 K [30]. Using an imported reactions mechanism (detailed in Table 2), the catalytic combustion of the gas with the platinum walls was modeled using the Laminar Finite-Rate Model. Once the simulation converged, species contours were generated and compared to the document to show accuracy (Figures 12 - 15):

By comparing the figures side by side, it can be seen that the created simulation matches the benchmark almost exactly. Additional figures have been included in Appendix A to further show this similarity (Figures 5 - 8) [9].
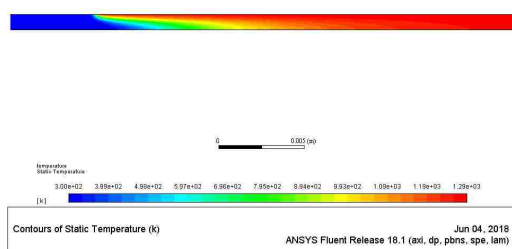
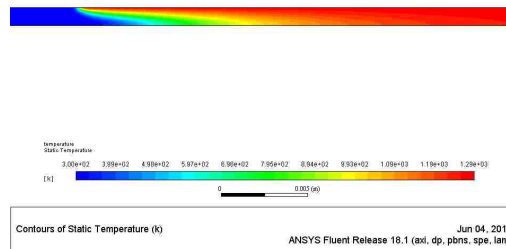Figure 12. Temp Contour of Reaction Zone from Personal Sim.

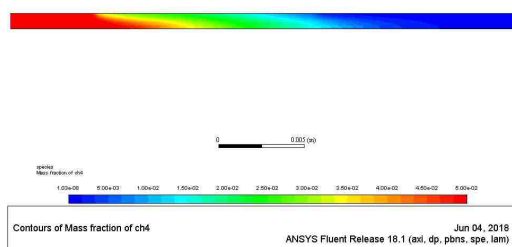Figure 13. Provided Temp Contour of Reaction Zone [9].

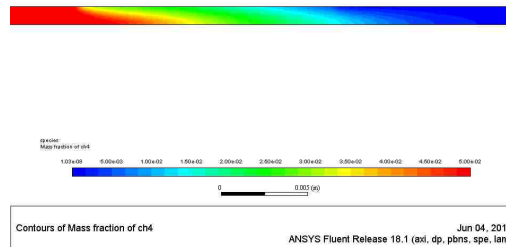Figure 14. Contour of CH_4 Reaction Zone from Personal Sim.

Figure 15. Provided Contour of CH_4 Reaction Zone [9].

0.3. MULTIPHASE FLOW

When modeling multiphase flows, especially using the Eulerian model, it is common (and sometimes necessary) to initialize the flow field using either a simpler model (such as the mixture model), lower order domain discretizations, or both. While the changing of discretization is a simple process, changing the complexity of the model can sometimes lead to residual divergence and failure to complete a simulation if it is not performed carefully and correctly, due to changes in phase interactions, solved equations, and possible effects on other models. Therefore, it was determined that a benchmark simulation that deals with these aspects was necessary.

In the benchmark simulation chosen, water and air both occupy a tee junction (Figure 16) affected by gravity and buoyancy, with a 2%/98% air/water mixture entering the bottom of the tee at 1.53 m/s. The top and right ends of the tee were modeled as outlets, with 62% of the escaping flow leaving the top, and 38% leaving the right side. The simulation was evaluated first using the Mixture Model with the Realizable $k-\epsilon$ turbulence model with the coupled solver and First-Order Discretization methods. Upon convergence, it was then solved at a higher order discretization, and lastly used as an initial solution for the Implicit Eulerian Method, as the recirculation of the flow is best captured using this more complex method [6].
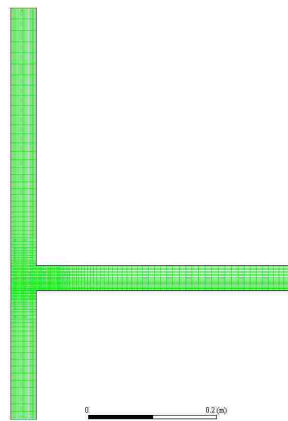
Figure 16. Mesh for Tee Junction Benchmark[6].

At the convergence of the Mixture and Eulerian methods, mass flux between the inlet and outlets was calculated to ensure proper convergence, followed by contours of velocity, volume fraction, and static pressure to be compared to the provided contours.

From the nearly identical figures (Figures 17 - 20, 9 - 16) and the Mass Flux imbalance values (0.001585% and 0.000958% for Mixture and Eulerian, respectively), the simulation was determined to be correct.

Figure 17. Provided Mixture v_f Contour[6].

Figure 18. Computed Mixture v_f Contour.
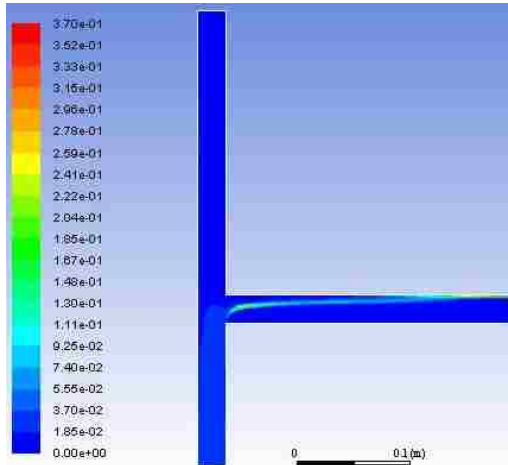

Figure 19. Provided Eulerian v_f Contour[6].
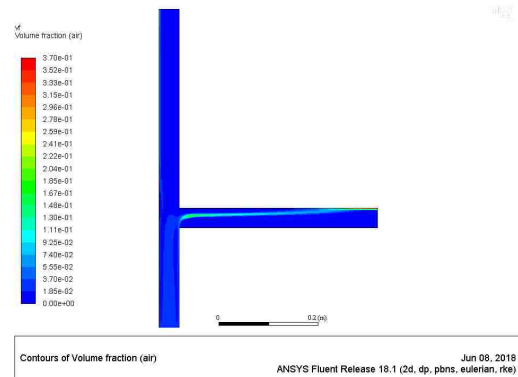
Figure 20. Computed Eulerian v_f Contour.

0.3.1. Heterogeneous Reactions. Due to the extra complexity complexity added through the addition of heterogeneous reactions in not only the solving, but also the setup of the simulation, it was determined that a benchmark case featuring just these was necessary, in addition to the other species transport benchmarks.

In the chosen benchmark, Transient, Turbulent Eulerian-Granular multiphase flow was used to simulate and analyze the combustion of solid coal particles in a gas-filled 2D riser [3] affected by gravity (Figure 21). The two phases consisted of two mixtures, with the primary being a gaseous mixture of O_2, N_2, CO, CO_2, and H_2O, and the secondary solid coal

Figure 21. Mesh of the 2D Riser.

made of of 2% C_s, 2% *volatiles*, H_2O_l, and *ash-coal*, where the *volatiles* and *ash-coal* were custom defined species, and the other species were taken from the FLUENT database. The simulation has two heterogeneous reactions, one for devolatilization, and one for char combustion, with reaction rates defined through provided UDFs, and one homogeneous reaction of carbon monoxide 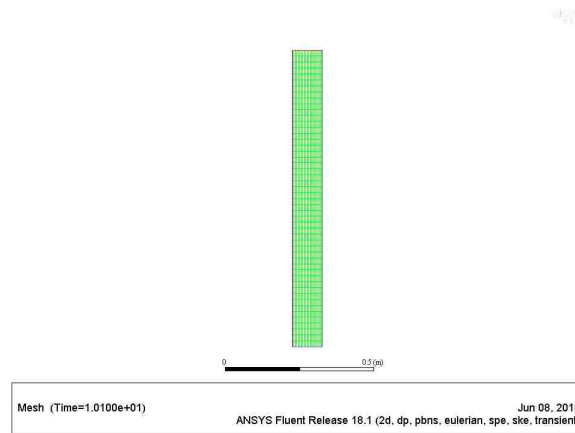becoming carbon dioxide [3]. While this reaction mechanism is simplified, it provides a good benchmark for the setup and execution of a heterogeneous reaction model simulation. As the simulation was transient, and therefore governed by the number of time steps input, the convergence was not solely dependent upon the residuals. Because of this, an additional convergence criteria was monitored in the form of the volume-average volume fraction of the secondary phase (Figures 22 and 23). It was determined that when this value became steady, the bulk of the reaction had reached equilibrium, and the time step could be made larger. The simulation was run for 100 time steps at 0.001 sec per time step to reach this steady value, and then 0.01 sec per step for 1000 more steps. Upon completion of the final time step, contours of mean values of properties were generated to compare to the contours of the original file (Figures 24 and 25).

While there is excellent agreement between Figures 22 and 23, there is some disparity between the contours in Figures 24 and 25. After careful comparison of the case setup and evaluation of the two cases, it was determined that the most likely cause was the ANSYS
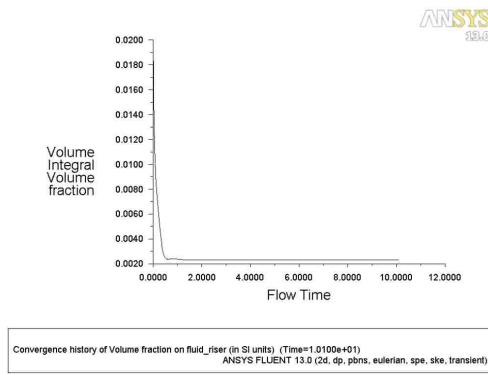
Figure 22. Provided v_f Convergence History [3].
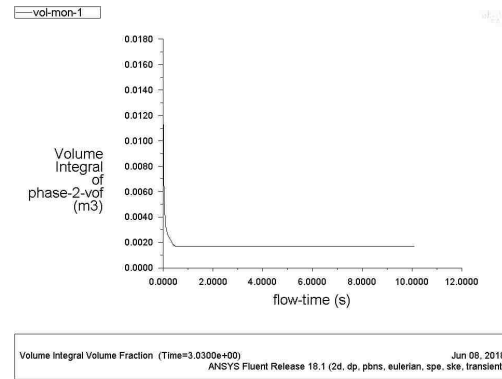
Figure 23. Calculated v_f Convergence History.

Fluent version, as the original contour comes from ANSYS 13.0, and the generated contour comes from ANSYS 18.1. As the new versions come with updates and improvements to various models and equations, it is likely that the difference in models caused the slight disparity.
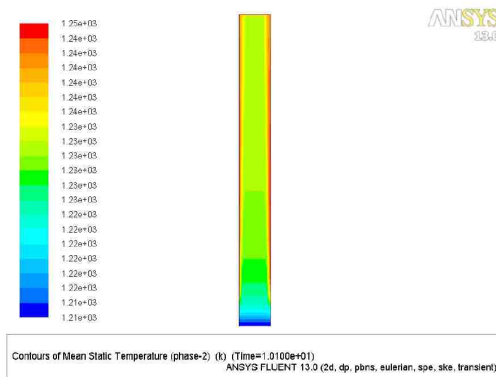
Figure 24. Provided Mean Temperature Contour.
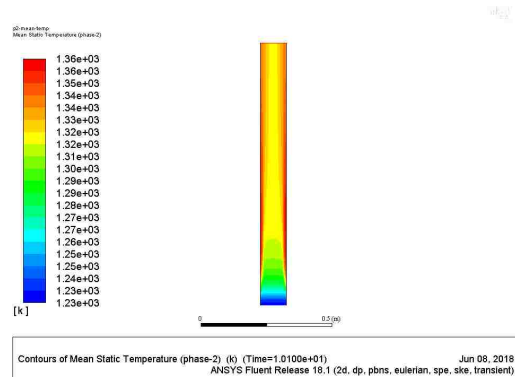
Figure 25. Generated Mean Temperature Contour.

APPENDIX B.

FIGURES AND TABLES

1. ADDITIONAL FIGURES
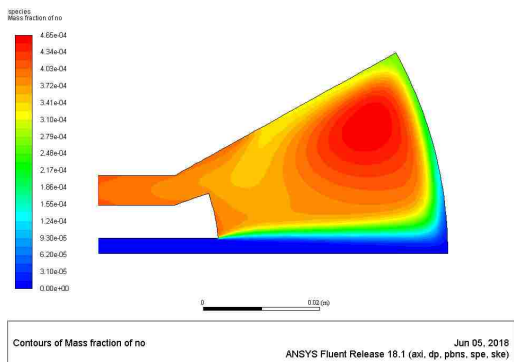
Figure 1. *NO* Contour from Generated Sim.
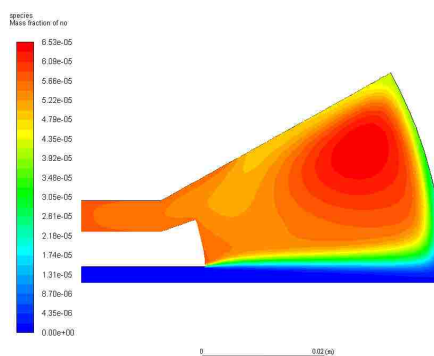
Figure 2. Provided *NO* Contour.
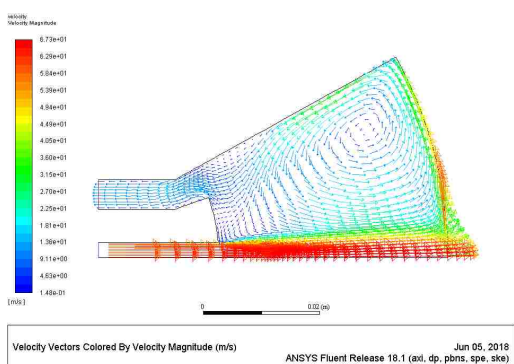
Figure 3. Velocity Vector Map from Generated Sim.
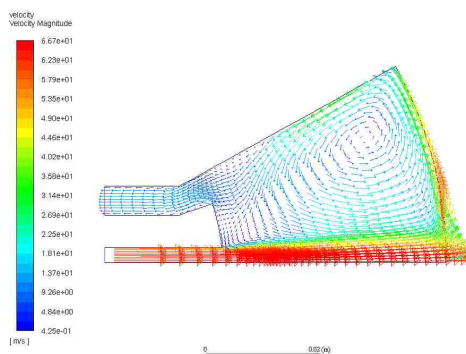
Figure 4. Provided Velocity Vector Map.
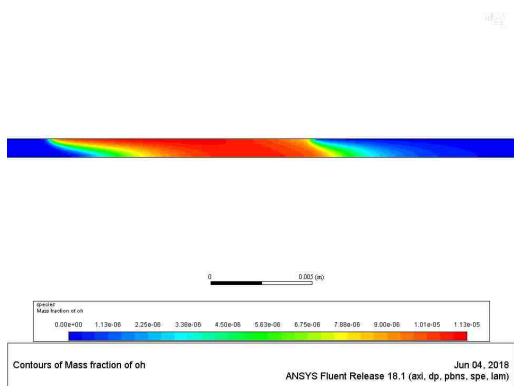
Figure 5. Contour of *OH* Reaction Zone from Personal Sim.
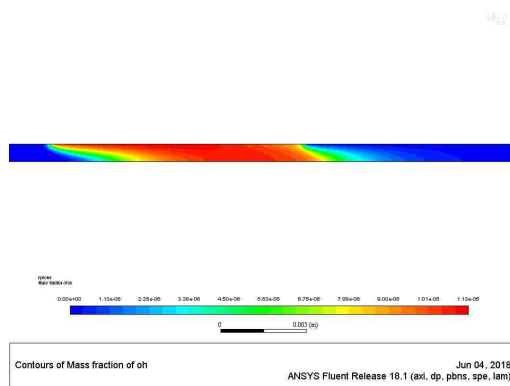
Figure 6. Provided *OH* Contour of Reaction Zone.
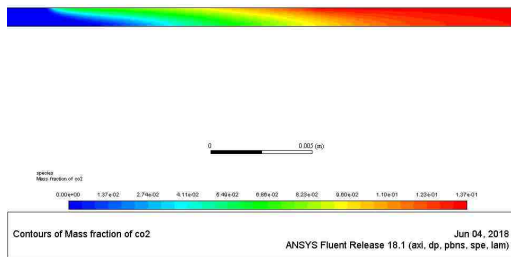
Figure 7. Contour of H_2O Reaction Zone from Personal Sim.
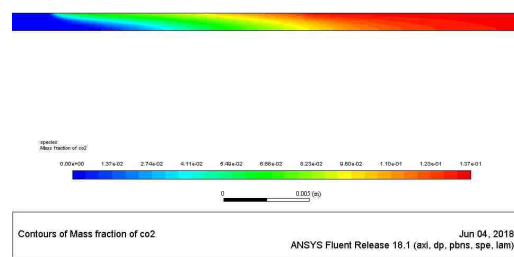
Figure 8. Provided $H2O$ Contour of Reaction Zone.
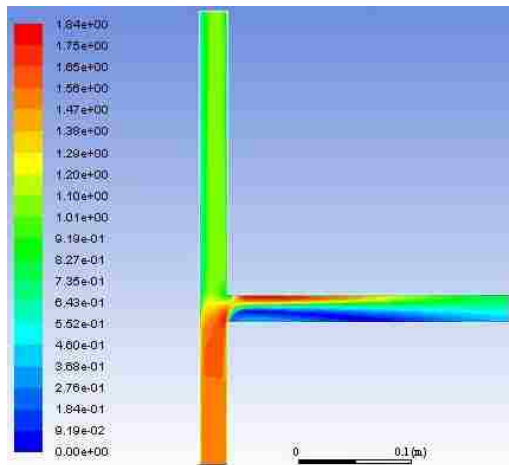
Figure 9. Provided Mixture Velocity Contour[6].
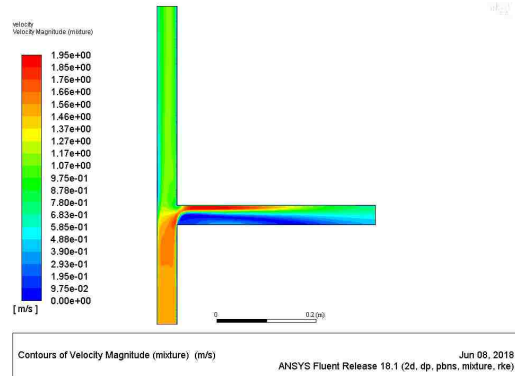
Figure 10. Computed Mixture Velocity Contour.
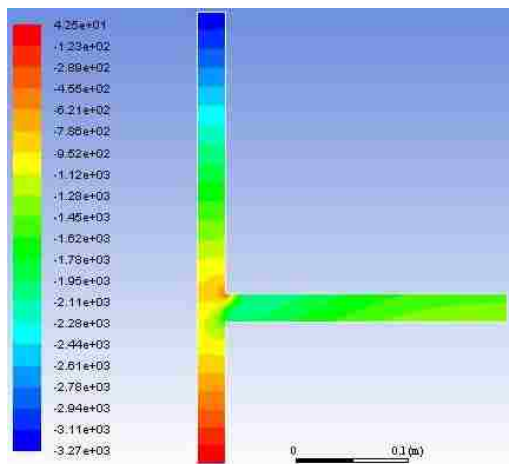
Figure 11. Provided Mixture Pressure Contour[6].
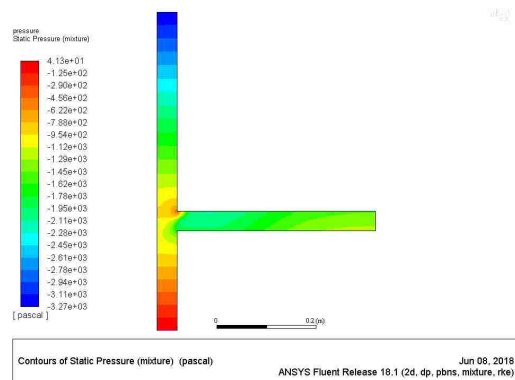
Figure 12. Computed Mixture Pressure Contour.
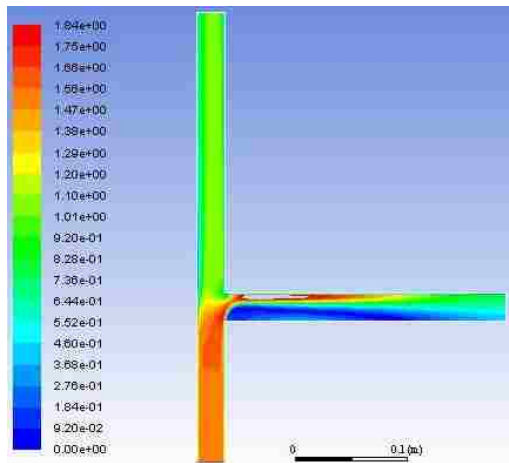
Figure 13. Provided Eulerian Velocity Contour[6].
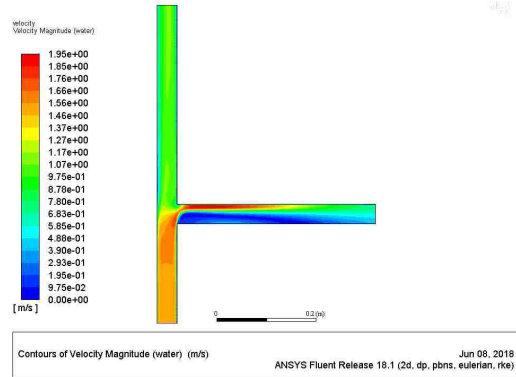
Figure 14. Computed Eulerian Velocity Contour.
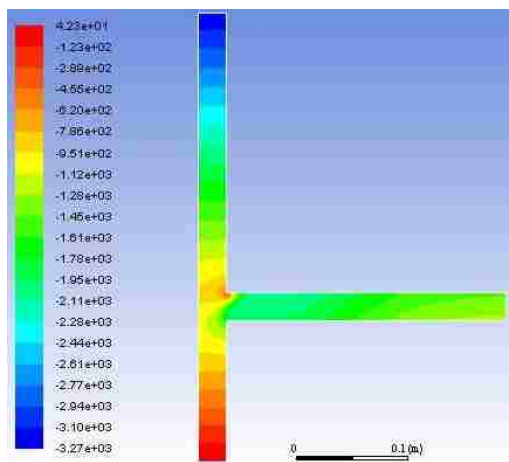
Figure 15. Provided Eulerian Pressure Contour[6].
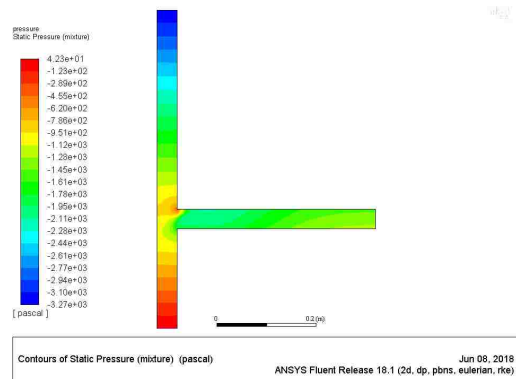
Figure 16. Computed Eulerian Pressure Contour.

2. ADDITIONAL TABLES

Table 1. Reaction Mechanism for Volumetric Reaction Benchmark Case.

Rxn	Reactants	v'	η'	Arr. Rate	Products	v''	η''	Mixing Rate
1	CH_4	1	1.46	$A_r = 1.6596e{+}15$	CO	1	0	Default Values
	O_2	1.5	0.5217	$E_r = 1.72e{+}08$	H_2O	2	0	
2	CO	1	1.6904	$A_r = 7.9799e{+}14$	CO_2	1	0	Default Values
	O_2	0.5	1.57	$E_r = 9.654e{+}07$				
3	CO_2	1	1	$A_r = 2.2336e{+}14$	CO	1	0	Default Values
				$E_r = 5.1774e{+}08$	O_2	0.5	0	
4	N_2	1	0	$A_r = 8.8308e{+}23$	NO	2	0	$A = 1e{+}11$[1]
	O_2	1	4.011	$E_r = 4.4366e{+}08$	CO	0	0	$B = 1e{+}11$
	CO	0	0.7211					
5	N_2	1	1	$A_r = 9.2683e{+}14$	NO	2	0	$A = 1e{+}11$
	O_2	1	0.5	$E_r = 5.7276e{+}08$				$B = 1e{+}11$
				$\beta_r = -0.5$				

[1] Here A and B represent turbulent mixing rates of the reactants and products, respectively.

Table 2. Reaction Mechanism Data for Catalytic Combustion Benchmark Case.

Rxn	Reactants	v'	η'	Arr. Rate	Products	v''	η''	Rev. Rxn?
1	H_2	1	1	$A_r = 4.4579e{+}07$	$H{<}s{>}$	2	0	
	$Pt{<}s{>}$[1]	2	1	$E_r = 0$				N
				$\beta_r = 0.5$				
2	$H{<}s{>}$	2	2	$A_r = 3.7e{+}20$	H_2	1	0	
				$E_r = 6.74e{+}20$	$Pt{<}s{>}$	2	0	N
3	O_2	1	1	$A_r = 1.8e{+}17$	$O{<}s{>}$	2	0	
	$Pt{<}s{>}$	2	2	$E_r = 0$				N
				$\beta_r = -0.5$				
4	O_2	1	1	$A_r = 2.01945e{+}14$	$O{<}s{>}$	2	0	
	$Pt{<}s{>}$	2	2	$E_r = 0$				N
				$\beta_r = -0.5$				
5	$O{<}s{>}$	2	2	$A_r = 3.7e{+}20$	O_2	1	0	
				$E_r = 2.132e{+}08$	$Pt{<}s{>}$	2	0	N
6	H_2O	1	1	$A_r = 2.395138e{+}08$	$H_2O{<}s{>}$	1	0	
	$Pt{<}s{>}$	1	1	$E_r = 0$				N
				$\beta_r = 0.5$				
7	$H_2O{<}s{>}$	1	1	$A_r = 1e{+}13$	H_2O	1	0	
				$E_r = 4.03e{+}07$	$Pt{<}s{>}$	1	0	N
8	OH	1	1	$A_r = 3.25934e{+}08$	$OH{<}s{>}$	1	0	
	$Pt{<}s{>}$	1	1	$E_r = 0$				N
				$\beta_r = 0.5$				
9	$OH{<}s{>}$	1	1	$A_r = 1e{+}13$	OH	1	0	N

Table 2. Reaction Mechanism Data for Catalytic Combustion Benchmark Case.

Rxn	Reactants	v'	η'	Arr. Rate	Products	v''	η''	Rev. Rxn?
				$E_r = 1.928e+08$	Pt<s>	1	0	
10	H<s>	1	1	$A_r = 3.7e+20$	OH<s>	1	1	Y
	O<s>	1	1	$E_r = 1.15e+07$	Pt<s>	1	1	
11	H<s>	1	1	$A_r = 3.7e+20$	H_2O<s>	1	1	Y
	OH<s>	1	1	$E_r = 1.74e+07$	Pt<s>	1	1	
12	OH<s>	2	2	$A_r = 3.7e+20$	H_2O<s>	1	1	Y
				$E_r = 4.82e+07$	O<s>	1	1	
13	CO	1	1	$A_r = 1.618e+16$	CO<s>	1	0	N
	Pt<s>	1	2	$E_r = 0$				
				$\beta_r = 0.5$				
14	CO<s>	1	1	$A_r = 1e+13$	CO	1	0	N
				$E_r = 1.255e+08$	Pt<s>	1	0	
15	CO_2<s>	1	1	$A_r = 1e+13$	CO_2	1	0	N
				$E_r = 2.05e+07$	Pt<s>	1	0	
16	CO<s>	1	1	$A_r = 3.7e+20$	CO_2<s>	1	0	N
	O<s>	1	1	$E_r = 1.05e+08$	Pt<s>	1	0	
17	CH_4	1	1	$A_r = 2.322201e+16$	CH_3<s>	1	0	N
	Pt<s>	2	2.3	$E_r = 0$	H<s>	1	0	
				$\beta_r = 0.5$				
18	CH_3<s>	1	1	$A_r = 3.7e+20$	$(CH_2)_s$<s>[2]	1	0	N
	Pt<s>	1	1	$E_r = 2e+07$	H<s>	1	0	
19	$(CH_2)_s$<s>	1	1	$A_r = 3.7e+20$	CH<s>	1	0	N
	Pt<s>	1	1	$E_r = 2e+07$	H<s>	1	0	
20	CH<s>	1	1	$A_r = 3.7e+20$	C<s>	1	0	N
	Pt<s>	1	1	$E_r = 2e+07$	H<s>	1	0	
21	C<s>	1	1	$A_r = 3.7e+20$	CO<s>	1	0	N
	O<s>	1	1	$E_r = 6.28e+07$	Pt<s>	1	0	
22	CO<s>	1	1	$A_r = 1e+17$	C<s>	1	0	N
	Pt<s>	1	1	$E_r = 1.84e+08$	O<s>	1	0	

[1] <s> denotes a site species

[2] $(\cdot)_s$ denotes a solid species

APPENDIX C.

CODES AND FUNCTIONS

1. ANSYS FLUENT UDFS

1.1. INSTRUCTIONS FOR IMPLEMENTING FLUENT UDFS

1. Ensure both Fluent files and any applicable UDFs are in the working directory

2. In Fluent, in the User Defined tab, select Functions, and from the drop down list select either interpreted or compiled, whichever method is desired.

   - If Interpreted UDF is selected:

      (a) Navigate to the desired UDF in the working directory.

      (b) Select Interpret, and allow time for the UDF to be interpreted.

   - If Compiled UDF is selected:

      (a) Select "Add..." and find the desired UDF in the working directory.

      (b) Give the library a name (the default is "libudf"), and select build.

      (c) Once the library finishes building, select "Load" and allow time for Fluent to load the UDF.

3. Navigate to the desired term you wish to replace with a UDF, and it should be selectable in the drop down menu of calculation type as the name of the function you provided.

1.2. BATCHSOURCE.C

```
1  #include "udf.h"
2
3  DEFINE_SOURCE(energy_source,c,t,dS,eqn)
4  {
5      real x[ND_ND];
6      real source;
7      real time;
8
9      time = CURRENT_TIME;
```

```
10    C_CENTROID(x,c,t);
11    if (time <= 3) /*Should only activate source term for first 3
      seconds */
12    {
13        if (x[0] <= 45e-3 && x[0] >= 42.75e-3 && x[1] >= 0 && x[1] <=
      2.741e-3)
14            /* Should restrict energy source to top 5% of vial */
15        {
16            source  = 1e9;
17            dS[eqn] = 0;
18        }
19        else
20        {
21            source  = 0;
22            dS[eqn] = 0;
23        }
24    }
25    else /*Turns off energy source after 3 sec */
26    {
27        source = 0;
28        dS[eqn] = 0;
29    }
30   return source;
31 }
```

1.3. MPARRHENIUS.C

```
1 /*
    ****************************************************************************

2    MPArrhenius.c
3    UDF for defining reaction mechanism for liquid propellant combustion
4 ****************************************************************************
    */
5
6 #include "udf.h"
7
8 /*Constants used in reaction calculations */
9
10 #define Ru 8.31434          /*Universal Gas Constant, J/mol-K */
11 #define kb 1.38064852e-23   /* Boltzmann Constant, J/K        */
12 #define A 2.14e10           /* Pre-Exponential Factor         */
13 #define Ea 10771            /*Activation Energy/kb, K          */
14
15 DEFINE_HET_RXN_RATE(PropWallComb,c,t,hr,mw,yi,rr,rr_t)
16 {
17    int phase_domain_index = 0;;
18    Thread **pt = THREAD_SUB_THREADS(t);
```

```c
19    Thread *prim_t = pt[0];                        /*Thread for Primary
      Phase     */
20    Thread *sec_t = pt[1];                         /*Thread for Secondary
      Phase   */
21    Domain *mixture_domain = Get_Domain(1);
22    Domain *subdomain = DOMAIN_SUB_DOMAIN(mixture_domain,
      phase_domain_index);
23    cell_t cell;
24    real T_prim = C_T(c,prim_t);                   /*Primary Phase Temp, K
          */
25    real T_sec = C_T(c,sec_t);                     /*Secondary Phase Temp,
      K     */
26    real diam = C_PHASE_DIAMETER(c,sec_t);        /*Secondary Phase
      Diameter     */
27    real y_prop = C_YI(c,sec_t,0);                 /*Mass Fraction of
      Propellant */
28    real rho_sec = C_R(c,sec_t);                   /*Density of Secondary
      Phase   */
29    real C_prop = y_prop*rho_sec/126;      /* Calculates Concentration of
       Prop */
30    real volfrac = C_VOF(c,sec_t);
31    real x[ND_ND];
32
33    /* Loops over all subdomains in the superdomain */
34    sub_domain_loop(subdomain,mixture_domain,phase_domain_index)
35    {
36        if (DOMAIN_ID(subdomain) == 3) /*Loops over only secondary (
      liquid) phase*/
37        {
38        /* Loops over all cell threads in secondary phase */
39        thread_loop_c (sec_t,subdomain)
40        {
41            /* Loops over all cells in secondary phase cell threads */
42            begin_c_loop_all (cell,sec_t)
43            {
44            C_CENTROID(x,cell,sec_t);
45            if (x[1] >=1.9e-4) /*Only allows reactions within 5% of the
      wall rxns */
46            {
47                *rr = A*exp(-Ea/T_sec)*C_prop*volfrac;    /*Calculates
      Reaction Rate   */
48            }
49            else
50            {
51                /* *rr = A*exp(-Ea/T_sec)*C_prop*volfrac*(x[1]/(2e-4));
      */
52                *rr = 0;
53            }
54            }
55            end_c_loop_all (cell,sec_t)
56        }
57        }
58    }
59 }
```

1.4. SOURCE.C

```c
/*************************************************************************
    UDF for defining Mass Source Term in Microtube
*************************************************************************/

#include "udf.h"

DEFINE_SOURCE(mass_source,c,t,dS,eqn)
{
    real x[ND_ND];
    real source;

    C_CENTROID(x,c,t);
    if (x[0] < 0.005) /* Should check if cell x coord is less than 0.005
     */
    {
        /* source = 3.41305e7; */
        source  = 30218.5903295646;
        dS[eqn] = 0;
    }
    else
    {
        source  = 0;
        dS[eqn] = 0;
    }

  return source;
}

DEFINE_SOURCE(co_source,c,t,dS,eqn)
{
    real x[ND_ND];
    real source;

    C_CENTROID(x,c,t);
    if (x[0] < 0.005) /* Should check if cell x coord is less than 0.005
     */
    {
        /* source = 3.41305e7; */
        source  = 0.2925*30218.5903295646;
        dS[eqn] = 0;
    }
    else
    {
        source  = 0;
        dS[eqn] = 0;
    }

  return source;
}
```

```
48
49 DEFINE_SOURCE(cos_source,c,t,dS,eqn)
50 {
51     real x[ND_ND];
52     real source;
53
54     C_CENTROID(x,c,t);
55     if (x[0] < 0.005) /* Should check if cell x coord is less than 0.005
        */
56     {
57         /* source = 3.41305e7; */
58         source  = 0.0037*30218.5903295646;
59         dS[eqn] = 0;
60     }
61     else
62     {
63         source  = 0;
64         dS[eqn] = 0;
65     }
66
67   return source;
68 }
69
70 DEFINE_SOURCE(co2_source,c,t,dS,eqn)
71 {
72     real x[ND_ND];
73     real source;
74
75     C_CENTROID(x,c,t);
76     if (x[0] < 0.005) /* Should check if cell x coord is less than 0.005
        */
77     {
78         /* source = 3.41305e7; */
79         source  = 0.1486*30218.5903295646;
80         dS[eqn] = 0;
81     }
82     else
83     {
84         source  = 0;
85         dS[eqn] = 0;
86     }
87
88   return source;
89 }
90
91 DEFINE_SOURCE(h2_source,c,t,dS,eqn)
92 {
93     real x[ND_ND];
94     real source;
95
96     C_CENTROID(x,c,t);
97     if (x[0] < 0.005) /* Should check if cell x coord is less than 0.005
        */
98     {
```

```
99          /* source = 3.41305e7; */
100         source   = 0.0211*30218.5903295646;
101         dS[eqn] = 0;
102     }
103     else
104     {
105         source   = 0;
106         dS[eqn] = 0;
107     }
108
109   return source;
110 }
111
112 DEFINE_SOURCE(h2o_source,c,t,dS,eqn)
113 {
114     real x[ND_ND];
115     real source;
116
117     C_CENTROID(x,c,t);
118     if (x[0] < 0.005) /* Should check if cell x coord is less than 0.005
        */
119     {
120         /* source = 3.41305e7; */
121         source   = 0.2568*30218.5903295646;
122         dS[eqn] = 0;
123     }
124     else
125     {
126         source   = 0;
127         dS[eqn] = 0;
128     }
129
130   return source;
131 }
132
133 DEFINE_SOURCE(h2s_source,c,t,dS,eqn)
134 {
135     real x[ND_ND];
136     real source;
137
138     C_CENTROID(x,c,t);
139     if (x[0] < 0.005) /* Should check if cell x coord is less than 0.005
        */
140     {
141         /* source = 3.41305e7; */
142         source   = 0.0499*30218.5903295646;
143         dS[eqn] = 0;
144     }
145     else
146     {
147         source   = 0;
148         dS[eqn] = 0;
149     }
150
```

```
151    return source;
152 }
153
154 DEFINE_SOURCE(n2_source,c,t,dS,eqn)
155 {
156     real x[ND_ND];
157     real source;
158
159     C_CENTROID(x,c,t);
160     if (x[0] < 0.005) /* Should check if cell x coord is less than 0.005
        */
161     {
162         /* source = 3.41305e7; */
163         source  = 0.2207*30218.5903295646;
164         dS[eqn] = 0;
165     }
166     else
167     {
168         source  = 0;
169         dS[eqn] = 0;
170     }
171
172   return source;
173 }
174
175 DEFINE_SOURCE(s2_source,c,t,dS,eqn)
176 {
177     real x[ND_ND];
178     real source;
179
180     C_CENTROID(x,c,t);
181     if (x[0] < 0.005) /* Should check if cell x coord is less than 0.005
        */
182     {
183         /* source = 3.41305e7; */
184         source  = 0.0067*30218.5903295646;
185         dS[eqn] = 0;
186     }
187     else
188     {
189         source  = 0;
190         dS[eqn] = 0;
191     }
192
193   return source;
194 }
195
196 DEFINE_SOURCE(mom_source,c,t,dS,eqn)
197 {
198     real x[ND_ND];
199     real source;
200
201     C_CENTROID(x,c,t);
```

```
202    if (x[0] < 0.005) /* Should check if cell x coord is less than 0.005
       */
203    {
204        source = 1356.25619836955;
205        /* source  = 20;*/
206        dS[eqn] = 0;
207    }
208    else
209    {
210        source  = 0;
211        dS[eqn] = 0;
212    }
213
214  return source;
215 }
216
217 DEFINE_SOURCE(energy_source,c,t,dS,eqn)
218 {
219    real x[ND_ND];
220    real source;
221
222    C_CENTROID(x,c,t);
223    if (x[0] <= 0.005) /* Should check if cell x coord is less than
       0.005 */
224    {
225        source  = 8.75e+10;
226        /* source = 211273891623.006;*/
227        dS[eqn] = 0;
228    }
229    else
230    {
231        source  = 0;
232        dS[eqn] = 0;
233    }
234
235  return source;
236 }
```

2. MATLAB CODES

2.1. MICROTUBEAPPROX.M

```
1 clc
2 close all
3 clear all
4
5 %
```

```matlab
 6 % This code is designed to approximate the change in u and P from the
 7 % decomposition and phase change of the liquid propellant as it moves down
 8 % the thruster tube. the values obtained are a rough approximation at best,
 9 % and should only be used as ballpark references in the final simulation.
10 % The equations used are a simplifed form of the Continuity and Navier
11 % Stokes to approximate the u and P after combustion, and then Fanno Flow
12 % to approximate the values at the outlet of the tube.
13 %─────────────────────────────────────────────────────────────────────

14
15 %Global Constants and Properties
16 D = 4e−4; %m
17 A = pi/4*D^2; %m^2
18 Ru = 8314; %J/kmol−K
19 kb = 1.68e−23; %J/K
20 Hreac = −1.6398e+09; %J/kg, calculated via AFT
21 Tcomb = 1903.34; %K, Cacl. via NASA_CEA
22 L = ;
23 n = 500; %No. of Steps
24 c = pi*D; %Circumference, m
25 CombZone = linspace(0.01*L,L,n)'; %Vector of size of comb zone, m

26
27 % Initial (Liquid) Properties
28 rho1 = 1530; %kg/m^3
29 T1   = 450;   %K
30 P1   = 200*101325/14.7; %Pa
31 u1   = 0.12; %m/s
32 Re1  = rho1*u1*D/0.1125; %Unitless
33 Cf1  = 16/Re1;
34 mdot = rho1*u1*A; %kg/s
35 Vdot = mdot/rho1;
36 MW1  = 126; %kg/kmol
37 R1   = Ru/MW1; %J/kg−K
38 Cp1 = 759.524; %J/kg−K
39 y1 = Cp1/(Cp1−R1);

40
41 % Post Combustion (Gas) Properties (via NASA_CEA)
42 rho2 = 1.8141; %kg/m^3
43 T2   = Tcomb;
44 y2   = 1.2341;
45 MW2  = 20.819; %kg/kmol
46 R2   = Ru/MW2; %J//kg−K
47 Cp2  = 2170.9; %J/kg−K
48 uson = 968.5; %m/s
49 Vdot2 = mdot/rho2;
50 mu2 = 1.47696e−5; %Calculated using the Herning and Zipperer Model for a
51                   %mixture of gases

52
53 %Tracked Variable Matrix Initialization
54 LFanno = zeros(n,1);
55 P2     = zeros(n,1);
56 Pe     = zeros(n,1);
57 ue     = zeros(n,1);
58 umax   = zeros(n,1);
59 Klimit = zeros(n,1);
```

```matlab
60  K       = zeros(n,1);
61  Me      = zeros(n,1);
62  Te      = zeros(n,1);
63  Pi      = zeros(n,1);
64
65  % Combustion Zone Approximation
66  u2  = rho1*u1/rho2;
67  Re2 = rho2*u2*D/mu2;
68  Cf2 = 16/Re2;
69  %As the pressure change depends on the surface area affected, it must go in
70  %the loop with the fanno flow calculations
71  for i = 1:n
72      Pi(i) = P1;
73      LFanno(i) = L-CombZone(i);
74      P2(i) = (mdot*(u1-u2) + P1*A + 0.5*rho1*u1^2*c*CombZone(i))/A;
75
76  %Fanno Calcs
77      M2 = u2/sqrt(y2*R2*T2);
78      if M2 < 0.3 %Incompressible, use Poiseuille Flow
79          Pe(i) = P2(i) - 8*mu2*LFanno(i)*u2/((D/2)^2);
80          umax(i)   = 2*u2;
81          Klimit(i) = NaN;
82          K(i) = NaN;
83          Me(i) = M2;
84          Te(i) = T2;
85          ue(i) = Me(i)*sqrt(y2*R2*Te(i));
86      else %Compressible Flow
87          Klimit(i) = 4*Cf2*LFanno(i)/D;
88          FAN = (1-M2^2)/(y2*M2^2) + (y2+1)/(2*y2)*log(((y2+1)*M2^2)/...
89          (2*(1+(y2-1)/2*M2^2)));
90          K(i) = FAN-Klimit(i);
91          fun = @(M) (1-M^2)/(y2*M^2) + (y2+1)/(2*y2)*log(((y2+1)*M^2)/...
92              (2*(1+(y2-1)/2*M^2))) - K(i);
93          Me(i) = fzero(fun,M2);
94          Pe(i) = (M2/Me(i))*((1+(y2-1)/2*M2^2)/...
95              (1+(y2-1)/2*Me(i)^2))^0.5*P2(i);
96          Te(i) = (1+(y2-1)/2*M2^2)/(1+(y2-1)/2*Me(i)^2)*T2;
97          ue(i) = Me(i)*sqrt(y2*R2*Te(i));
98          umax(i) = NaN;
99      end
100     disp(i)
101 end
102
103 figure(1)
104 plot(CombZone./L,P2,'b')
105 hold on
106 plot(CombZone./L,Pe,'r')
107 hold on
108 plot(CombZone./L,Pi,'--k')
109 grid on
110 xlabel('%Length of Combustion Zone')
111 ylabel('Pressure, Pa')
112 legend('P2','Pe','Pi','Location','Best')
113
```

```
114  DP = Pi − Pe;
115
116  figure(2)
117  plot(CombZone./L,DP)
118  grid on
119  xlabel('%Length of Combustion Zone')
120  ylabel('Change in Pressure, Pa')
121
122  figure(3)
123  plot(CombZone./L,DP/101325*14.7)
124  grid on
125  xlabel('%Length of Combustion Zone')
126  ylabel('Change in Pressure, PSI')
```

2.2. SOURCE.M

```
1
2  clc
3  close all
4  clear all
5
6  %This code is designed to determine the source terms for a specific FLUENT
7  %simulation given the actual inlet conditions, and the expected outlet
8  %conditions.
9
10  %Knowns
11  Ru = 8314; %J/mol−K
12  u1 = 0.11; %m/s
13  rho1 = 1420; %kg//m^3
14  A = pi*(2e−4)^2; %m^2
15  P1 = 200*101325/14.7; %N/m^2
16  rho2 = 1.8141; %kg/m^3, alt. formulation used IGL
17  P2 = P1 − 40530; %Approx. Pressure Drop, N/m^2
18  % P2 = 1365137.52802304;
19  mdot2 = rho1*u1*A; %kg/s
20  T1 = 450;
21  T2 = 1900;
22  R1 = Ru/126; %J/kg−K
23  R2 = Ru/20.819; %J/kg−K
24  rho1_1 = P1/(R1*T1);
25  rho2_2 = P2/(R2*T2);
26  u2 = mdot2/(rho2*A);
27  Re1 = rho1*u1*4e−4/0.1125;
28  Cf = 16/Re1;
29  mdot1 = u1*A*rho1_1;
30  V = A*CZ; %Volume of affected area, m^3
31
32  %Enthalpy, Hreac Calcs
33  species = {'Propellant';'CO';'COS';'CO2';'H2';'H2O';'H2S';'N2';'S2'};
```

```matlab
34 mol     = [4.54; 6.018; 0.036; 1.946; 6.012; 8.214; 0.844; 4.54; 0.06];
35 [m,~]   = size(species);
36 h1      = PropCalc(T1,P1,1,'enthalpy','Propellant');
37 [~,~,~,~,~,hreac,~,MWprop,~,~]  = SpecLookup('Propellant',450);
38 hreac   = mol(1)*hreac*MWprop;
39 h2      = 0;
40 hprod   = 0;
41 for i = 2:m
42     [~,~,~,~,~,h,~,MW,~,~]  = SpecLookup(species{i},450);
43     hh = PropCalc(T2,P1,1,'enthalpy',species{i});
44     h2 = h2 + hh; %Enthalpy at 1900 K
45     hprod = mol(i)*h*MW + hprod; %Product H for Hreac\
46 end
47 Q = (hprod−hreac);
48
49 %Source Term Calcs
50 Smass = (mdot2−mdot1)/V
51
52 Smom  = (A*(P2−P1) − 0.5*rho1_1*u1^2*Cf*A + mdot2*u2 − mdot1*u1)/V
53
54 Se    = (mdot2*(h2 + u2^2/2) − mdot1*(h1 + u1^2/2) − Q*mdot1)/V
```

REFERENCES

[1] Thermal Decomposition Of Hydroxylamine Nitrate, volume 0872, 1988, doi:10.1117/12.943754.

[2] Ignition and combustion of the HAN-based liquid propellants, volume 1, CPIA Publication 557, 1990.

[3] Modeling Heterogeneous Reactions with Eulerian-Granular Flow, Canonsburg, PA, 2010.

[4] 'Advantages of Computational Fluid Dynamics,' `http://www.pretechnologies.com/services/computational-fluid-dynamics/advantage`, 2014, Accessed: 07-2018.

[5] ANSYS Fluent Theory Guide 18.1, Canonsburg, PA, 2017.

[6] ANSYS Fluent Tutorial Guide 18.0, Canonsburg, PA, 2017.

[7] ANSYS Fluent Users Guide 18.1, Canonsburg, PA, 2017.

[8] 'A Comparison of CFD Software Packages,' `https://www.resolvedanalytics.com/theflux/comparing-popular-cfd-software-packages`, 2017, Accessed: 06-2018.

[9] 'Mr CFD,' `https://www.mr-cfd.com/`, 2017, Accessed: 05-2018.

[10] 'Ansys Fluent,' `https://www.ansys.com/products/fluids/ansys-fluent`, 2018, Accessed: 06-2018.

[11] Amrousse, R., Katsumi, T., Itouyama, N., Azuma, N., Kagawa, H., Hatai, K., Ikeda, H., and Hori, K., 'New HAN-based mixtures for reaction control system and low toxic spacecraft propulsion subsytem: Thermal decomposition and possible thruster applications,' Combustion and Flame, 2015, **162**, pp. 2686–2692.

[12] Berg, S. P., Development of Ionic Liquid Multi-Mode Spacecraft Micropropulsion Systems, Ph.D. thesis, Missouri University of Science and Technology, Rolla, MO, 2015.

[13] Berg, S. P., Coleman, B., and Rovey, J. L., 'Decomposition of Ionic Liquid Ferrofluids for Multi-Mode Spacecraft Propulsion,' in '50th AIAA/ASME/SAE/ASEE Joint Propulsion Conference,' American Institute of Aeronautics and Astronautics, Cleveland, OH, 2014 doi:10.2514/6.2014-3568.

[14] Berg, S. P. and Rovey, J. L., 'Dual-Mode Propellant Properties and Performance Analysis of Energetic Ionic Liquids,' in '50th AIAA Aerospace Sciences Meeting,' American Institute of Aeronautics and Astronautics, Nashville, TN, 2012 .

[15] Berg, S. P. and Rovey, J. L., 'Ignition Evaluation of Monopropellant Blends of HAN and Imidazole-Based Ionic Liquid Fuels,' in '50th AIAA Aerospace Sciences Meeting,' American Institute of Aeronautics and Astronautics, Nashville, TN, 2012 doi: 10.2514/6.2012-974.

[16] Berg, S. P. and Rovey, J. L., 'Performance Analysis of an Integrated Multi-Mode Chemical Monopropellant Inductive Plasma Thruster,' in '49th AIAA/ASME/SAE/ASEE Joint Propulsion Conference,' American Institute of Aeronautics and Astronautics, San Jose, CA, 2013 doi:10.2514/6.2013-3956.

[17] Berg, S. P. and Rovey, J. L., 'Assessment of Multi-Mode Spacecraft Micropropulsion Systems,' in '50th AIAA/ASME/SAE/ASEE Joint Propulsion Conference,' American Institute of Aeronautics and Astronautics, Cleveland, OH, 2014 doi: 10.2514/6.2014-3758.

[18] Berg, S. P. and Rovey, J. L., 'Decomposition of a Double Salt Ionic Liquid Monopropellant on Heated Metallic Surfaces,' in '52nd AIAA/SAE/ASEE Joint Propulsion Conference,' American Institute of Aeronautics and Astronautics, Salt Lake City, UT, 2016 doi:10.2514/6.2016-4578.

[19] Berg, S. P. and Rovey, J. L., 'Assessment of Multimode Spacecraft Micropropulsion Systems,' Journal of Spacecraft and Rockets, 2017, **54**(3), pp. 592–601, doi:10.2514/1.A33649.

[20] Berg, S. P. and Rovey, J. L., 'Decomposition of Double Salt Ionic Liquid Monopropellant in a Microtube for Multi-Mode Micropropulsion Applications,' in '53rd AIAA/SAE/ASEE Joint Propulsion Conference,' American Institute of Aeronautics and Astronautics, Atlanta, GA, 2017 doi:10.2514/6.2017-4755.

[21] Bergman, T. L., Lavine, A. S., Incropera, F. P., and Dewitt, D. P., Introduction to Heat Transfer, 6th Ed., John Wiley and Sons, Inc., Hoboken, NJ, 2011.

[22] Boyarko, G. A., Sung, C. J., and Schneider, S. J., 'Catalyzed combustion of hydrogen-oxygen in platinum tubes for micro-propulsion applications,' Proceedings of the Combustion Institute, 2005, pp. 2481–2488.

[23] Chambreau, S. D., Popolan-Vaida, D. M., Vaghjiani, G. L., and Leone, S. R., 'Catalytic Decomposition of Hydroxylammonium Nitrate Ionic Liquid: Enhancement of NO Formation,' Journal of Physical Chemistry Letters, 2017, **8**(10), doi:10.1021/acs.jpclett.7b00672, pMID: 28438020.

[24] Chen, J., Wang, Q., Pan, J., and He, Z., 'Study on catalytic combustion of hydrogen inside micro tube,' Advanced Materials Research, 2011, **339**, pp. 265–270, doi:10.4208/www.scientific.net/AMR.339.265.

[25] Chen, J., Yan, L., and Song, W., 'Numerical simulation of micro-scale catalytic combustion characteristics with detailed chemical kinetic reaction mechanisms of hydrogen/air,' Reaction Kinetics, Mechanisms and Catalysis, 2014, **113**, pp. 19–37, doi:10.1007/s11144-014-0719-x.

[26] Decker, M. M., Freedman, N. K. E., Leveritt, C. S., and Wojciechowski, J. Q., 'HAN-Based Liquid Gun Propellants: Physical Properties,' Technical report, US Army Ballistic Research Laboratory, 1987, report No. BRL-TR-2864.

[27] Dominick, S., 'Design, Development, and Flight Performance of the Mars Global Surveyor Propulsion System,' 1999 35th AIAA Joint Propulsion Conference.

[28] Donius, B. R. and Rovey, J. L., 'Analysis and Prediction of Dual-Mode Chemical and Electric Ionic Liquid Propulsion Performance,' in '48th Aerospace Sciences Meeting,' American Institute of Aeronautics and Astronautics, Orlando, FL, 2010 .

[29] Hass, J. M. and Holmes, M. R., 'Multi-Mode Propulsion System for the Expansion of Small Satellite Capabilities,' 2010.

[30] Jafarinia, A., Modeling Catalytic Combustion of Methane Using Wall Surface Reactions, 2017.

[31] Jafarinia, A., Premixed Flow in a Conical Chamber using the Finite-Rate Chemistry Model, 2017.

[32] Lee, H. S. and Litzinger, T. A., 'Chemical kinetic study of han decomposition,' Combustion and Flame, 2003, **135**, pp. 151–169.

[33] Mundahl, A. J., Berg, S. P., Rovey, J. L., Huang, M., Woelk, K., Wagle, D. V., and Baker, G., 'Characterization of a Novel Ionic Liquid Monopropellant for Multi-Mode Propulsion,' in '53rd AIAA/SAE/ASEE Joint Propulsion Conference,' American Institute of Aeronautics and Astronautics, Atlanta, GA, 2017 doi:10.2514/6.2017-4756.

[34] Nicol, D. G., A Chemical and Numerical Study of NOx and Pollutant Formation in Low-Emissions Combustion, Ph.D. thesis, University of Washington, 1995.

[35] Ranjan, R., Karthikeyan, K., Riaz, F., and Chou, S. K., 'Cold gas propulsion microthruster for feed gas utilization in micro satellites,' Applied Energy, 2018, **220**, pp. 921–933, doi:https://doi.org/10.1016/j.apenergy.2018.03.040.

[36] Rumpfkeil, M. P., 'Computational Fluid Dynamics,' https://pdfs.semanticscholar.org/presentation/4106/e6007172daa24f9e4d794bd086752907684a.pdf, 2014.

[37] Sassé, R. A., 'Thermal Characteristics of Concentrated Hydroxylammonium Nitrate Solutions,' Technical report, US Army Ballistic Research Laboratory, 1988, report No. BRL-MR-3651.

[38] Sassé, R. A., 'Analysis of Hydroxylammonium Nitrate Based Liquid Propellants,' Technical report, US Army Ballistic Research Laboratory, 1990, report No. BRL-TR-3154.

[39] Sassé, R. A., Davies, M. A., Fifer, R. A., Decker, M. M., and Kotlar, A. J., 'Density of Hydroxylammonium Nitrate Solutions,' Technical report, US Army Ballistic Research Laboratory, 1988, report No. BRL-MR-3720.

[40] Shabanian, S. R., Rahimi, M., Khoshhal, A., and Alsairafi, A. A., 'Cfd Study on Hydrogen-Air Premixed Combustion in a Micro Scale Chamber,' Iranian Journal of Chemistry and Chemical Engineering, 2010, **29**(4), pp. 161–172.

[41] Volchko, S. J., Sung, C. J., Huang, Y., and Schneider, S. J., 'Catalytic Combustion of Rich Methane/Oxygen Mixtures for Micropropulsion Applications,' Journal of Propulsion and Power, 2006, **22**(3).

[42] White, F. M., Viscous Fluid Flow, 3rd Ed., McGraw-Hill, New York, 2006.

[43] Wilcox, D. C., Basic Fluid Mechanics, 5th Ed., DCW Industries, La Canada, CA, 2012.

[44] Yan, Y., Tang, W., Zhang, L., Pan, W., Yang, Z., Chen, Y., and Lin, J., 'Numerical simulation of the effect of hydrogen addition fraction on catalytic micro-combustion characteristics of methane-air,' International Journal of Hydrogen Energy, 2014, **39**, pp. 1864–1873.

VITA

Andrew Paul Taylor was born in St. Louis in 1993. He attended school in the Bayless School District in Affton, MO, up until his undergraduate studies, which took place at the Missouri University of Science and Technology starting in the fall of 2012. He graduated Summa Cum Laude with a Bachelors of Science in Aerospace Engineering in May 2016, and began graduate school the following fall. In December 2018, he received his MS degree in Aerospace Engineering from Missouri University of Science and Technology.